microbial biotechnology

Open Access

A structurally unique *Fusobacterium nucleatum* tannase provides detoxicant activity against gallotannins and pathogen resistance

José Miguel Mancheño,[1] Estíbaliz Atondo,[2] Julen Tomás-Cortázar,[2,3] José Luís Lavín,[4,†] Laura Plaza-Vinuesa,[5] Itziar Martín-Ruiz,[2] Diego Barriales,[2] Ainhoa Palacios,[2] Claudio Daniel Navo,[6] Leticia Sampedro,[2] Ainize Peña-Cearra,[2,7] Miguel Ángel Pascual-Itoiz,[2] Janire Castelo,[2] Ana Carreras-González,[2] Donatello Castellana,[8] Aize Pellón,[2] Susana Delgado,[9] Patricia Ruas-Madiedo,[9] Blanca delas Rivas,[5] Leticia Abecia,[2,7] Rosario Muñoz,[5] Gonzalo Jiménez-Osés,[6] Juan Anguita[2,10,*] and Héctor Rodríguez[2]

[1]*Departamento de Cristalografía y Biología Estructural, Instituto de Química-Física "Rocasolano" (IQFR-CSIC), Madrid, 28006, Spain.*

[2]*Inflammation and Macrophage Plasticity lab, CIC bioGUNE-BRTA (Basque Research and Technology Alliance), Derio, 48160, Spain.*

[3]*UCD Conway Institute, University College of Dublin, Belfield, Dublin 4, D04 V1W8, Ireland.*

[4]*Bioinformatics Unit, CIC bioGUNE-BRTA, Bizkaia Technology Park, Derio, Bizkaia 48160, Spain.*

[5]*Laboratorio de Biotecnología Bacteriana, Instituto de Ciencia y Tecnología de los Alimentos y Nutrición (ICTAN)-Consejo Superior de Investigaciones Científicas (CSIC), Madrid, 28006, Spain.*

[6]*Computational Chemistry lab, CIC bioGUNE-BRTA, Derio, 48160, Spain.*

[7]*Department of Immunology, Microbiology and Parasitology, Faculty of Medicine and Nursing, Universidad del País Vasco/Euskal Herriko Unibertsitatea, Leioa, 48940, Spain.*

[8]*Research & Development, CIC bioGUNE-BRTA, Derio, 48160, Spain.*

[9]*Dairy Research Institute, Spanish National Research Council (Instituto de Productos Lácteos de Asturias - CSIC), Asturias, 33300, Spain.*

[10]*Ikerbasque, Basque Foundation for Science, Bilbao, 48013, Spain.*

Received 9 August, 2020; revised 27 November, 2020; accepted 28 November, 2020.

*For correspondence. E-mail janguita@cicbiogune.es); Tel. 8610-15091284067; Fax. 86+02987091130.

†Present address: Neiker, Parque Tecnológico de Bizkaia, Derio, Spain.

Microbial Biotechnology (2022) **15**(2), 648–667
doi:10.1111/1751-7915.13732

Funding Inforamtion

Supported by grants from the Spanish Ministry of Science and Innovation (MCI) cofinanced with FEDER funds (SAF2015-65327-R and RTI2018-096494-B-100 to JA; AGL2017-86757-R to LA, SAF2015-73549-JIN to HR; RTI2018-099592-B-C22 to GJO) and the Mizutani Foundation for Glycoscience (200077 to GJO). LA and GJO are supported by the Ramon y Cajal program (RYC-2013-13666 and RYC-2013-14706 respectively). JTC and AP are the recipients postdoctoral fellowships from the Basque Government. DB is the recipient of a MCI FPI fellowship. APC is the recipient of a fellowship from the University of the Basque Country. We thank the MCI for the Severo Ochoa Excellence accreditation (SEV-2016-0644) and the Basque Department of Industry, Tourism and Trade (Etortek and Elkartek programs). JMM thanks the ALBA synchrotron for providing access time to the BL-13 XALOC beamline. This work is supported by grants from the Jesús de Gangoiti Barrera Foundation.

Summary

Colorectal cancer pathogenesis and progression is associated with the presence of *Fusobacterium nucleatum* and the reduction of acetylated derivatives of spermidine, as well as dietary components such as tannin-rich foods. We show that a new tannase orthologue of *F. nucleatum* ($TanBF_{nn}$) has significant structural differences with its *Lactobacillus plantarum* counterpart affecting the flap covering the active site and the accessibility of substrates. Crystallographic and molecular dynamics analysis revealed binding of polyamines to a small cavity that connects the active site with the bulk solvent which interact with catalytically indispensable residues. As a result, spermidine and its derivatives, particularly N^8-acetylated spermidine, inhibit the hydrolytic activity of $TanBF_{nn}$ and increase the toxicity of gallotannins to *F. nucleatum*. Our results support a model in which the balance between the detoxicant activity of $TanBF_{nn}$ and the presence of metabolic inhibitors can dictate either conducive or unfavourable conditions for the survival of *F. nucleatum*.

Introduction

Fusobacterium are anaerobic, gram-negative bacteria known for a long time as pathogens linked to oral diseases. In the last decade, several studies have also noted the presence of *F. nucleatum* outside its usual oral

cavity niche its association with colorectal cancer (CRC) (Kostic *et al*., 2013; Rubinstein *et al*., 2013; Yachida *et al*., 2019). Intriguingly, *F. nucleatum* increased tumour multiplicity in a mouse model of intestinal tumorigenesis (Kostic *et al*., 2013). Although the biological explanation of the carcinogenic effect of this bacterium remains elusive, potential underlying mechanisms are the generation of a pro-inflammatory microenvironment through recruitment of immune cells, in particular macrophages, and different oncogenic responses predominantly mediated by the FadA adhesin (Brennan and Garrett, 2019). New studies have also pointed to *F. nucleatum* as both a key species that allows CRC early stage detection and as a bad prognostic biomarker of CRC survival (Zeller *et al*., 2014; Mima *et al*., 2016; Yamaoka *et al*., 2018). A recent study has described the presence of *F. nucleatum* and its accompanying microbiome in distal metastases of CRC. Moreover, the treatment of mice-bearing colon cancer xenografts with antibiotics specific for *F. nucleatum* resulted in decreased bacterial loads, diminished cancer proliferation and delayed tumour growth (Bullman *et al*., 2017). These studies underscore the importance of this tumour-associated pathogen during disease development and progression.

Detrimental *F. nucleatum* expansion and activity in the intestine might be associated with nutritional determinants, since diet is recognized as one of the most important environmental risk factors for CRC (Mehta *et al*., 2017). Understanding the microbial metabolism of dietary components is critical to comprehend gut ecological dynamics in response to the diet. Phenolics and gallotannins, in particular, are relevant components of the chemical composition of some fruits and raw vegetables, which affect their organoleptic properties and health effects (Barbieri *et al*., 2017). These compounds are transformed within the gut due to the action of a vast array of microbial enzymatic activities, rendering some metabolites with antimicrobial activity, such as pyrogallol or phloroglucinol (Kolodzeij *et al*., 1999; Buzzini *et al*., 2008; Redondo *et al*., 2014). These antimicrobial metabolites might affect microbial ecosystems and therefore *F. nucleatum* settlement and expansion. The role of other diet-related metabolites such as biogenic amines remains almost completely unexplored in relation to *F. nucleatum* dynamics. However, some studies have postulated a potential participation of spermidine and putrescine in CRC (Soda, 2011; Madeo *et al*., 2018).

Among the enzymes that play a critical role in the release of bioactive compounds from gallotannins, tannases are essential due to their role as first-line degradative enzymes of high molecular weight gallotannins, making these compounds accessible for subsequent downstream transformation (Jimenez *et al*., 2014b). Tannases are esterases present in different microorganisms that are capable of breaking the ester bonds (esterase activity) and depside bonds (depsidase activity) of gallic acid (Haslam and Stangroom, 1966). However, although different microbial tannase enzymes have been described and characterized (de Las Rivas *et al*., 2019), including the *F. nucleatum* subsp. *polymorphum* tannase, $TanB_{Fnp}$ (Tomás-Cortázar *et al*., 2018), studies addressing their prevalence and their role in human microbiota ecosystems are lacking. Despite the implications of these proteins in diet–bacteria interactions, functional and structural studies of bacterial tannases of gut pathogens or relevant microorganisms in the gut environment are missing. To date, only one bacterial tannase belonging to the probiotic bacterium, *Lactobacillus plantarum* $TanA_{Lp}$, has been structurally characterized (Ren *et al*., 2013; Wu *et al*., 2013).

Here, we describe and characterize a new tannase from *F. nucleatum* subsp. *nucleatum* ($TanB_{Fnn}$) and study its distribution among the bacteria taxa present in a human cohort as well as the prevalence and abundance of tannase orthologues in the human population. Furthermore, we show that $TanB_{Fnn}$ is active against phenolic compounds when present in the culture medium and propose the adaptative advantage through gallotannin detoxification as the origin of the high prevalence of these genes in CRC-associated oral pathobionts. In order to get a deeper understanding of the mechanism of action of $TanB_{Fnn}$, we solved its crystal structure, which permitted the identification of previously unknown regulatory mechanisms of the enzymatic activity for this group of proteins. Based on structural information as well as enzymatic assays and molecular dynamics simulations, we describe the interaction of the enzyme with the biogenic amine spermidine and its acetylated derivatives. These data unveil the inhibitory interactions that modulate the survival of *F. nucleatum* in the presence of gallotannins.

Results

Tannase is a core protein in human microbiota and might be relevant for niche adaptation of oral pathogens

Since its initial description in *Staphylococcus lugdunensis*, the presence of tannase activity in bacteria has been repeatedly linked to CRC-associated microorganisms (Noguchi *et al*., 2007; Lopez de Felipe *et al*., 2014). However, the importance of this enzyme for human disease has not been addressed to date. The increased abundance of tannase orthologues among bacteria species that are overrepresented in CRC has been hypothesized (Lopez de Felipe *et al*., 2014) as well as the elevated presence of oral microorganisms in tumours (Flemer *et al*., 2018). We first assessed the presence of gene orthologues for the tannase gene (using the

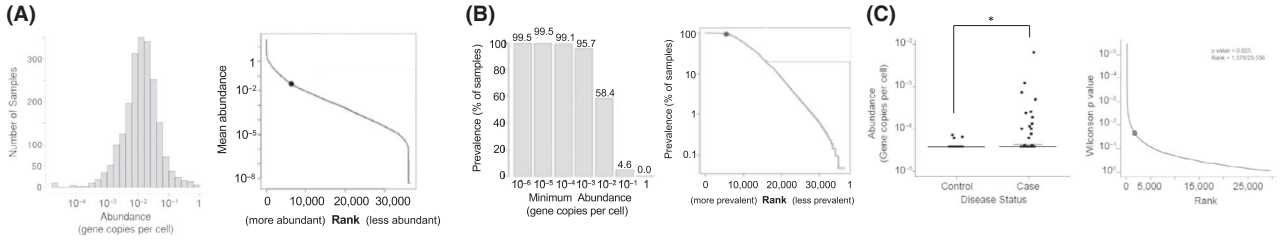

Fig. 1. Estimated abundance of tannase proteins across 1267 human gut metagenomes in a human cohort.A. Estimated average tannase copies per cell and ranking position of the mean abundance of tannase proteins across the whole metagenome.B. Percentage of samples (prevalence) among human gut metagenomes with a determined minimum abundance.C. Abundance (gene copies per cell) in control population individuals and CRC disease patients in a CRC disease cohort. The average ± SD copies were 5.8 x 10^{-6} ± 1.9 x 10^{-5} for the control group and 1.6 x 10^{-4} ± 8.2 x 10^{-4} for the CRC group. *Wilcoxon rank-sum test, $P = 0.025$.

previously characterized *L. plantarum* tannase lp_2956, *tanL* -UniProt ID: F9US92_LACPL-, as reference and 30% of identity as the minimum threshold), using metagenomic faecal data from 1872 individuals sampled in six countries across three continents (Nayfach *et al*., 2015). Species harbouring orthologous tannase proteins were detected in several bacterial genera present in the oral niche that are associated with CRC (Flynn et al., 2016; Bullman *et al*., 2017), including *Fusobacterium, Veillonella, Aggregatibacter, Selenomonas* and *Mitsuokella* (Table S1). Furthermore, the analysis of the abundance of tannase orthologues showed that this gene was present in most of the analysed populations (Fig. 1A), with a mean abundance among samples of 0.03 gene copies per eukaryotic cell. Therefore, tannases can be considered core genes of the human microbiota, although their abundance is variable across the population. Furthermore, we found that 95.7% of the population harbours at least 1 gene copy per 1000 eukaryotic cells (Fig. 1B).

We have recently cloned and characterized a tannase from *F. nucleatum* subsp. *polymorphum,* a clinically relevant *Fusobacterium* subspecies, $TanB_{Fnp}$ (Tomás-Cortázar *et al*., 2018). We then proceeded to the identification and cloning of the gene encoding a homologous tannase enzyme ($TanB_{Fnn}$) from *F. nucleatum* subsp. *nucleatum* 23726, due to the relevance of this microorganism in CRC development and progression (Liu *et al*., 2019). Figure S1 shows a schematic representation of the genetic context of the $tanB_{Fnn}$gene within the *F. nucleatum* genome. We also determined the abundance of highly similar (> 80%) orthologues of the *F. nucleatum* subsp. *nucleatum* tannase in a set of CRC patients and healthy individuals (Feng *et al*., 2015). CRC patients showed a significantly higher abundance of tannase orthologues than the control group (P value = 0.025; Fig. 1C), suggesting a positive correlation between this enzyme and the disease.

$TanB_{Fnn}$ is capable of degrading dietary gallotannins and provides protection against their toxicity

Mounting evidence indicates a role for tannase activity in the adaptation of oral pathogens to the oral niche, an environment rich in phenolic compounds (Jimenez, 2014). More importantly, a putative role for microbial adaptation to the CRC niche when phenolics reach the gut has also been demonstrated (Reveron *et al*., 2013). To further explore the adaptive implications of $TanB_{Fnn}$, the enzyme was studied in detail. The coding gene was cloned into *Escherichia coli*, and the activity of the purified protein (Fig. S2) was tested. HPLC analysis confirmed that $TanB_{Fnn}$ is an esterase, active against different food substrates including wine and tea gallotannins as well as gallic acid esters used as additives in the food industry (Fig. S3). $TanB_{Fnn}$ was active against a great variety of simple and complex tannins rendering gallic acid (GA) as the sole product in most of the cases. The biochemical characterization of the enzyme showed maximal activity at 30°C in a range of pH between 6 and 7 (Fig. S4), which is very similar to the behaviour of $TanB_{Fnp}$ (Tomás-Cortázar *et al*., 2018), as expected due to their high amino acid sequence identity (93%).

We next studied the capacity of the bacteria to transform gallotannins in culture. Simple and complex gallotannins were added to *F. nucleatum* cultures, and the supernatants were subsequently analysed by HPLC after 7 days. As with the purified enzyme, both simple and complex tannins were totally or partially hydrolysed, rendering GA as the main product (Fig. 2A). The capacity of the cultured bacteria to degrade compounds unable to enter the bacterial cell, such as tannic acid, plus the presence of a signal peptide in the protein sequence confirmed the existence of an active extracellular tannase in the *F. nucleatum* cultures. In order to ascertain the potential role of the tannase activity in diet

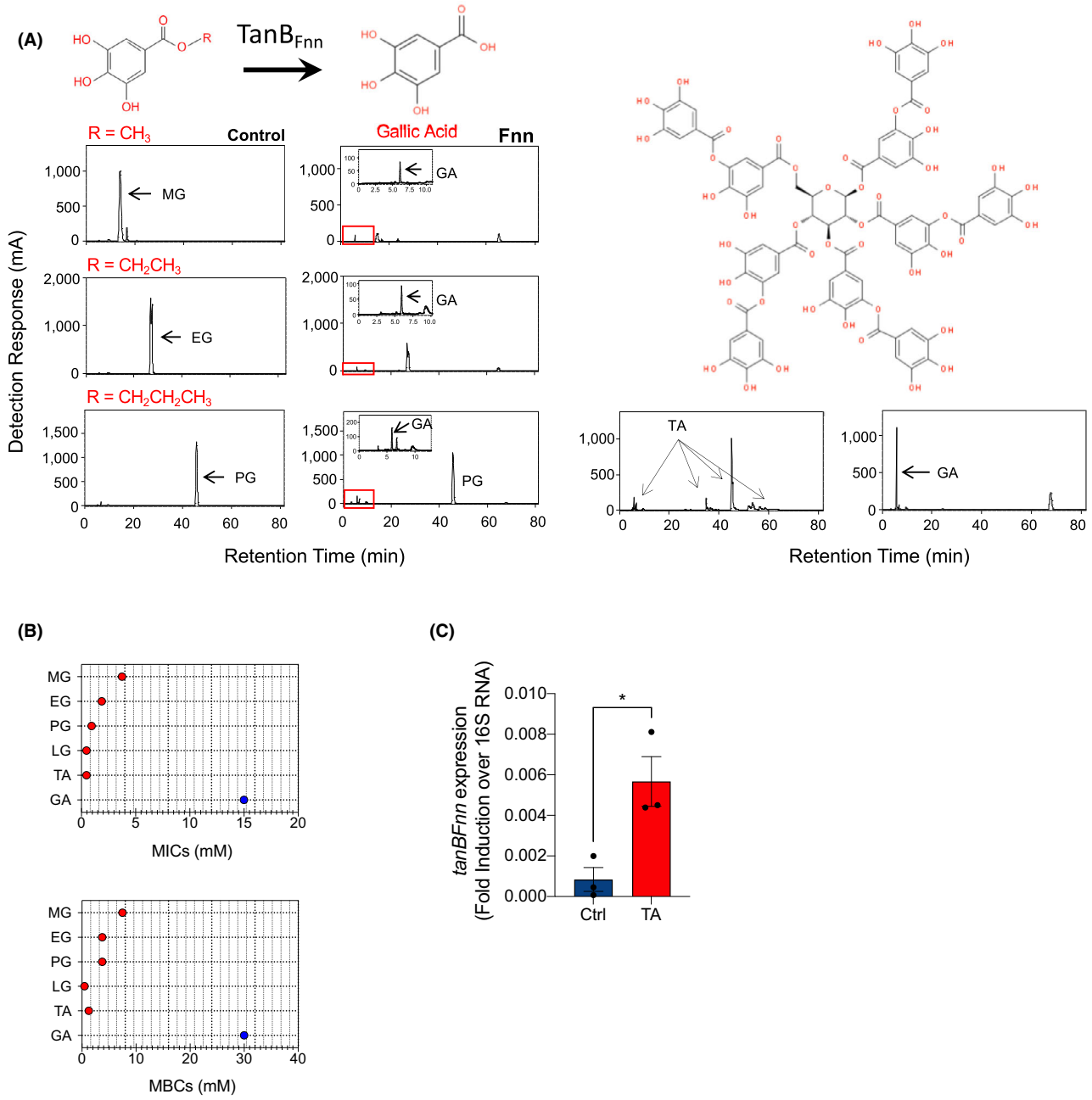

Fig. 2. Tannase is active against high and low molecular weight gallotannins.A. HPLC chromatograms showing gallotannins incubated in vehicle or in the presence of *F. nucleatum* subsp. *nucleatum* (Fnn) growing cells. The basic enzymatic reaction is depicted at the top.B. Minimum inhibitory concentrations (MICs, top) and minimum bactericidal concentrations (MBCs, bottom) of different gallotannins (MG-Methyl Gallate, EG-Ethyl Gallate, PG-Propyl Gallate, LG-Lauryl gallate, TA-Tannic Acid) and GA-Gallic acid (the main product of tannase activity over gallotannin compounds) for *F. nucleatum* subsp. *nucleatum*.C. *TanB$_{Fnn}$* gene expression induction by spermidine in *F. nucleatum*. Mid-log cultures of *F. nucleatum* were incubated for 10 min with 0.1 mM tannic acid. The bacteria were then analysed for *TanB$_{Fnn}$* gene expression levels by real-time PCR. Gene expression levels were calculated relative to the 16S rRNA gene. The results represent the average ± of three independent cultures. *Student's *t*-test, $P < 0.05$.

component detoxification, we determined the minimum inhibitory concentrations (MICs) and the minimum bactericidal concentrations (MBCs) of the substrates and products of the enzyme. *F. nucleatum* tolerated much higher concentrations of GA in the medium than simple and complex gallotannins (Fig. 2B). Bacterial growth was not inhibited in the presence of gallic acid concentrations up to 15 mM, while all dietary substrates inhibited the

growth of the bacteria in concentrations ranging from 0.47 to 3.75 mM. Similarly, the analysis of MBCs showed that all gallotannin substrates induced a much higher toxic activity than GA on *F. nucleatum*. On the other hand, the analysis by real-time PCR of the expression level of $TanB_{Fnn}$ in *F. nucleatum* exposed to tannic acid showed its upregulation after 10 min of incubation (Fig. 2C), showing that the bacterium responds to the presence of the toxicant increasing the expression of the tannase gene. Overall, these results suggested a detoxification role of the enzyme.

Crystal structure of $TanB_{Fnn}$

We solved the crystal structure of $TanB_{Fnn}$ by molecular replacement using the atomic coordinates of the tannase from *Lactobacillus plantarum* WCFS1 as a search model (PDB code: 4J0D; 42% sequence identity). Details from the crystallographic studies are provided in Experimental Procedures, and data collection and refinement statistics are shown in Table 1.

Table 1. Crystallographic data collection and refinement statistics.

Parameter	$TanB_{Fnn}$
Data collection statistics	
Wavelength (Å)	0.97926
Space group	P 2_1
Unit cell dimensions	
a, b, c (Å)	71.84, 91.07, 124.07
α, β, γ (°)	90, 101.696, 90
Temp (K)	100
X-ray source	Synchrotron
Resolution range[a] (Å)	47.79-(2.46-2.40)
No. unique reflections	60,889 (6,014)
Completeness	99.1 (97.8)
Multiplicity	6.5 (6.6)
$R_{p.i.m.}$[b]	0.074 (0.319)
$\langle I/\sigma(I)\rangle$	13.3 (3.7)
CC1/2[c]	0.981 (0.874)
Refinement statistics	
Resolution range (Å)	47.79-2.40
R_{work}/R_{free}[d]	0.17/0.25
No. of atoms	
Protein	11,264
Water	407
Other	31
RMS deviations	
Bond length (Å)	0.008
Bond angles (°)	0.99
Ramachandran plot	
Favoured/outlier (%)	94.80/0.56
Monomers per AU	3
PDB code	6YQ4

a. Values between parentheses correspond to the highest resolution shells.

b. R_{pim} measures the precision of averaged intensities. Rp.i.m.=($\sum$-hkl1n − 1$\sum$i = 1nIi(hkl)−<I(hkl)>)/($\sum$hkl$\sum$i = 1nIi(hkl)), where Ii(hkl) is the i^{th} measurement of reflection hkl, <I(hkl)> is the weighted mean of all measurements, and n is the redundancy for the hkl reflection.

c. CC1/2 is the correlation coefficient between intensity estimates from half data sets.

d. R_{work} = ($\sum$hkl|Fo − Fc|)/$\sum$|Fo|, where *Fo* is the observed structure factor amplitude and *Fc* the calculated value. The R_{free} value is calculated identically but using a small subset (5%) of randomly selected reflections that are set aside from the beginning and not used in the refinement of the structural model.

The three independent protein molecules within the asymmetric unit of the $TanB_{Fnn}$ crystal were essentially indistinguishable (the maximum root-mean-square deviation – r.m.s.d. – for 478 alpha carbon (Cα) positions is 0.69 Å). Analysis of the crystal protein packing with PISA (Krissinel and Henrick, 2007) indicated the absence of oligomeric assemblies, in agreement with our gel filtration observations showing that $TanB_{Fnn}$ is monomeric in solution (Fig. S2).

$TanB_{Fnn}$ belongs to the α/β-hydrolase superfamily (Nardini, 1999; Ollis et al., 1992), which is structurally characterized by a central and almost parallel eight-stranded β-sheet surrounded by five α helices, two located in the concave side of the sheet (α2 and α17) and three in the convex side (α3, α4 and α12). Insertions of new strands (one at the N-terminal end for $TanB_{Fnn}$) or large domains, mainly located at the C-terminal end of strands, are well tolerated by this central core (Nardini, 1999). For $TanB_{Fnn}$, a large insertion appeared between strands β7 and β14 comprising the residues 207-438, which amounts to 47% of all its residues.

A search for structural homologues with the DALI server (Holm and Rosenstrom, 2010) revealed that the tannase from *Lactobacillus plantarum* WCFS1 ($TanA_{Lp}$) is the closest structural homologue of $TanB_{Fnn}$ (r.m.s.d. = 2.7 Å for 458 Cα atoms). Nevertheless, despite this overall structural similarity, superimposition of both structures revealed the existence of large, local structural deviations between them, both within the α/β-hydrolase core and in the inserted domain (Fig. 3). Surprisingly, the largest structural deviation affected the flap covering the active site of the enzyme, together with modifications in the adjacent β4-α2 and β1-β2 connecting loops. These structural differences are remarkable since, when taken as a whole, reveal an unexpected complexity in the way tannases work (see below). Finally, $TanB_{Fnn}$ contained an insertion of a 19 residue stretch (residues 391-409) (Fig. S5A), which as indicated above, is only partially observed in the electron density map, most probably due to its intrinsic flexibility.

The catalytic machinery of $TanB_{Fnn}$ and $TanA_{Lp}$ was found to be strictly conserved (Fig. S5B). The residues forming the catalytic triad in $TanB_{Fnn}$ correspond to Ser^{166}, His^{476} and Asp^{444}, respectively, and those which would interact with the three hydroxyl groups of ethyl gallate (EG), Asp^{446}, Lys^{351} and Glu^{365} (Ren *et al.*, 2013). Interestingly, Asp^{444} from the catalytic triad in $TanB_{Fnn}$ is stabilized by a 2.8 Å hydrogen bond with a

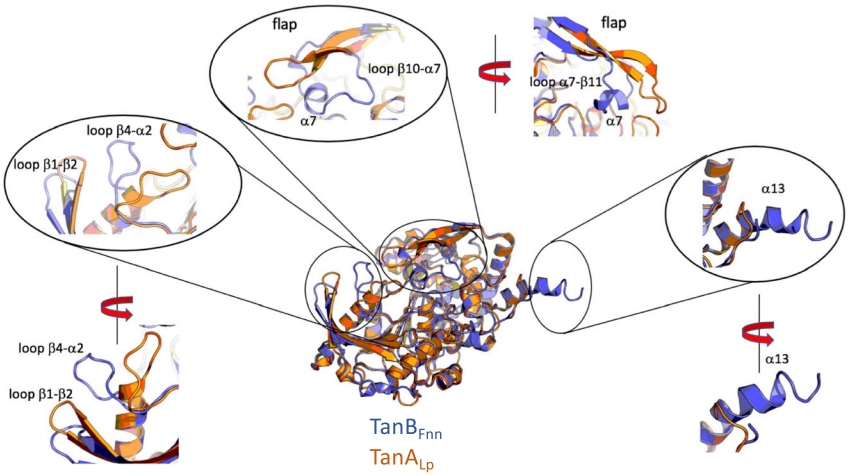

Fig. 3. Comparison of the three-dimensional structures of TanB$_{Fnn}$ and TanA$_{Lp}$. Superimposition of the structures of TanB$_{Fnn}$ (blue, ribbon model) and TanA$_{Lp}$ (orange, ribbon model) reveals significant differences between both protein predominantly found in the loops β1-β2 and β4-α2, in the flap region (in particular in the loops β10-α7 and α7-β11) and in the α13 helix (shown from left to right). For clarity, two opposite views are depicted for each distinct region.

water molecule, similarly to what is found in the structures of other esterases such as hormone-sensitive lipases (Hemila *et al.*, 1994; Alvarez *et al.*, 2014). Finally, the well-defined sphere of electron density observed in the α3-β8 connecting loop has been tentatively modelled as a Mg^{2+} ion since this provides the best agreement between *B*-factor values of neighbour atoms with the carboxylate moiety of the Asp^{150} side chain as the main protein–ligand for metal binding.

An active site blockage system in TanB$_{Fnn}$

The flap located over the active site of TanA$_{Lp}$ is formed by a long and twisted β-hairpin (strands β8 and β9) whose conformation results in the formation of an open tunnel (Fig. 4A) (Ren *et al.*, 2013). Most probably, this arrangement facilitates the catalytically competent binding of substrates such as tannic acid (TA) into the active site. Unlike TanA$_{Lp}$, the flap in TanB$_{Fnn}$ adopts a different conformation. It folds over the active site and covers both sides of the tunnel, resulting in the partial occlusion of the active site (Fig. 4B).

The flap in TanB$_{Fnn}$ is formed by a proximal, two short stranded β-sheets (strands β10 and β11) followed by two irregular regions and a distal, short helix (α7). As a result of this new conformation, the environment of catalytically essential residues changes, in particular those from the nucleophile Ser^{166} and the catalytically essential residue Asp^{446} (Fig. 4C). Hence, the OG atom of the side chain of Ser^{166} is located at hydrogen bond distance (3.7 Å) to the OD1 atom of the side chain of Asn^{244} from helix α7 of the flap, and the carboxyl group of Asp^{446} forms a strong ion pair with Arg^{246} that also belongs to the flap (distance of 2.2 Å between NH and OD2 atoms respectively). This interaction is facilitated since the guanidinium moiety of Arg^{246} is highly oriented towards Asp^{446} by a cation-π interaction with the aromatic ring of Phe^{234} and a 3.2 Å hydrogen bond between its NE nitrogen atom and the main chain carbonyl oxygen of Tyr^{243} (Fig. 4C). In addition, a large part of the substrate-binding site is occupied by the bulky side chains of Phe^{234} and Tyr^{243}, hindering the catalytically competent binding of big substrates.

The disappearance of the tunnel resulted from the new conformation of the irregular regions situated between strand β10 and helix α7 and between helix α7 and strand β11 respectively. With respect to TanA$_{Lp}$, the latter region moves towards the β15-α17 connecting loop, resulting in a partial closure of this side of the tunnel, whereas the first region approaches helix α12 and the loop between strands β5 and β6. Notably, this new arrangement results in the development of a small cavity (inner diameter of around 8 Å and 15 Å depth) that connects the active site and in particular, the nucleophile Ser^{166} and the side chains of the catalytically essential residues, Lys^{351} and Glu^{365}, with the bulk solvent. This explains the presence of a glycerol in the active site in a conformation that mimics the gallate-binding mode (Fig. S5B), similarly to TanA$_{Lp}$ (Matoba *et al.*, 2013). Remarkably, a region of elongated, well-defined electron density is observed along the cavity of one of the TanB$_{Fnn}$ independent molecules of the asymmetric unit (further details below), whereas in the other two molecules the equivalent density is discontinuous and hardly interpretable.

Since TanB$_{Fnn}$ is active against small substrates such as alkyl gallates and much larger substrates such as

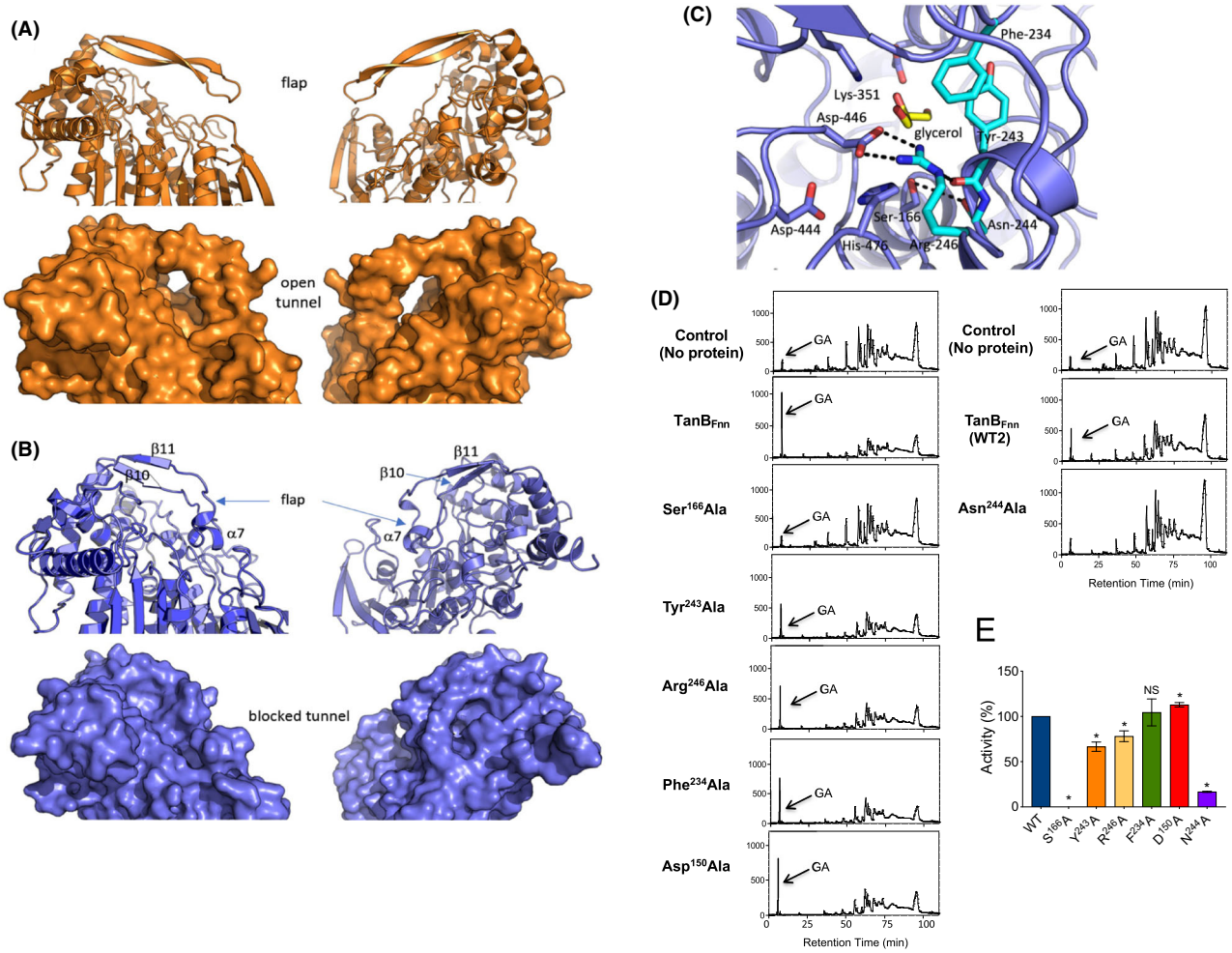

Fig. 4. Structural features of TanB$_{Fnn}$ and TanA$_{Lp}$ around the flap region.A. Opposite views of TanA$_{Lp}$ in orange ribbon (upper part) and solid surface (lower part) models, revealing the disposition of the flap over the active site of the enzyme, which results in the formation of a tunnel.B. Opposite views of TanB$_{Fnn}$ (in the same orientation as in A) in blue ribbon (upper part) and solid surface (lower part) models. The conformation of the flap results in the closure of the tunnel.C. Interactions between amino acid side chains of residues from the flap (cyan, sticks model) and catalytically essential residues of TanB$_{Fnn}$ (magenta, sticks model). The glycerol molecule within the active site is also shown (yellow, sticks model).D. Tannase activity of different single point mutants relative to the activity of the wild-type TanB$_{Fnn}$ protein. The panels represent HPLC chromatograms showing the activity of the wild-type protein and different variants against tannic acid.E. Relative activity of the TanB$_{Fnn}$ mutants over methyl gallate compared to the wild-type protein (WT). NS, not significant; *Student's *t*-test, $P < 0.05$. The bars represent the average ± SE of quadruplicates and correspond to one of 2–3 independent experiments performed.

tannic acid (TA), it is likely that its flap must change its conformation to permit their proficient binding of substrates of different sizes into the active site. Under this scenario, it is expected that residues from the flap occupying the substrate-binding site of TanB$_{Fnn}$ should leave this environment before the substrate gets into the active site and therefore would play either no direct role in catalysis or an ancillary one, although this does not exclude functional roles of these residues in the more open states of the enzyme. To get some light on these aspects, we generated the protein variants, Asp^{150}Ala, Ser^{166}Ala, Phe^{234}Ala, Tyr^{243}Ala, Asn^{244}Ala and Arg^{246}Ala, and determined their activity against both MG and TA. As expected, the mutation of the catalytically essential amino acid, Ser^{166}, rendered the protein inactive (Fig. 4D,E). On the other hand, the mutations Phe^{234}Ala and Asp^{150}Ala did not affect or enhanced slightly the activity of the enzyme, while the protein variant Asn^{244}Ala was almost inactive against both substrates. Finally, mutations in Tyr^{243} and Arg^{246} showed a slightly reduced activity levels against methyl gallate compared to the wild-type enzyme (> 75%) (Fig. 4E) and were also active against TA, producing GA (Fig. 4 D). Overall, these results indicate that although not catalytically essential, Tyr^{243} and Asn^{244} affect the extent of the hydrolytic activity of the enzyme likely by playing a

role in the stabilization of this flexible region of the enzyme. Indeed, both Tyr^{243} and Asn^{244} are highly conserved in tannases from other members of the order Fusobacteriales. Furthermore, the equivalent residue of Asn^{244} in TanALp (Asn^{238}) is located at the distal end of the shortened flap and in contact with the β4-α1 connecting loop (Ren *et al*., 2013), probably contributing to the stabilization of this region.

Apart from the large structural changes observed in the flap, three other regions of $TanB_{Fnn}$ clearly differ from those analogous in $TanA_{Lp}$. Two of them are in the vicinity of the flap: the segment comprised by residues Gly^{91} to Ala^{98} from the β4-α2 connecting loop and the short β1- β2 connecting loop. Relative to $TanA_{Lp}$, the first region in $TanB_{Fnn}$ moves more than 10 Å from the flap, which permits its closure, and the second one moves around 5 Å in the same direction (Fig. 3). As a whole, the new conformations of the flap and these two regions suggest the possibility of a concerted movement of all of them. Interestingly, the irregular region between helix α7 and strand β11 and the mentioned loops exhibit the highest *B*-factor values of the $TanB_{Fnn}$ structure, indicating high flexibility. Finally, the third region that clearly differs with respect to $TanA_{Lp}$ is helix α13 and the α13-α14 connecting loop (Fig. 3), which are structural features of tannases observed exclusively in the genus *Fusobacterium*, in particular, in *F. nucleatum*, *F. hwasookii* and *F. periodonticum*, being absent in *F. necrophorum* and *F. massiliense*. However, the current structure of $TanB_{Fnn}$ does not provide clues about a potential role of this last structural element in the function of the protein.

Molecular modelling of substrates bound to $TanB_{Fnn}$

The ability of $TanB_{Fnn}$ to bind polyphenolic substrates was investigated through microsecond molecular dynamics (MD) simulations. We used first a representative example of the small polyphenols experimentally tested, EG. The small size and lack of significant conformational flexibility of EG easily allowed its manual docking into $TanB_{Fnn}$ active site using the crystallographic structure of $TanA_{Lp}$ in complex with EG as a reference, even with its flap in a closed conformation (Fig. S6). It must be noted that, as described above, for the substrates to get into the active site, the flap must undergo very likely a conformational change into a more open state. The kinetic rate of these conformational transitions, as well as the population of the closed *vs*. open states in solution, might indeed affect the global reaction rate and the observed catalytic proficiency of the enzyme. This possibility is strongly supported by the reduction in tannase activity observed in the mutants described before, in which the conformational dynamics and thus the relative population of the open and closed states of the flap are likely affected. In this initial computer model, EG was bound mainly through hydrogen bond interactions between two of its three phenolic hydroxyl groups and Glu^{365} of $TanB_{Fnn}$. However, the significant width of the active site of this enzyme even with the large flap covering it precluded this pose to be maintained along different MD simulation runs, and fast reallocation of EG by non-persistent interactions with negatively charged residues Glu^{365} and Asp^{446} were observed (Fig. S6). In some of the trajectories, EG abandoned the active site and migrated to the bulk solvent after around 700 ns. These observations suggest that small phenolic esters, despite being able to enter the active site of $TanB_{Fnn}$ and undergo ester cleavage, might not be ideal substrates for this enzyme.

Methyl digallate (MDG) was modelled in a similar way to EG. This larger, conformationally flexible and more densely hydroxylated substrate allowed a much more stable binding to $TanB_{Fnn}$ active site. Thus, a single binding pose with multiple protein–ligand contacts was observed throughout the microsecond simulations (Fig. S7). Of note, the flexible flap opens up at the initial stages of the simulation and quickly closes over the substrate to keep it in a stable and potentially reactive orientation by means of aromatic stacking interactions with Tyr^{243}. This observation supports the reduced activity of the Tyr^{243}Ala mutant, likely by reduction of stabilizing interactions between the enzyme and the substrate. The simulated binding mode of MDG to $TanB_{Fnn}$ displays the substrate in a reactive near-attack conformation, in which the reacting ester group is optimally positioned for nucleophilic attack from the Ser^{166}-His^{476}-Asp^{444} catalytic triad. Negatively charged residues Glu^{365} and Asp^{446} stablish hydrogen bond interactions with the phenolic hydroxyl groups of the reacting fragment, contributing to the proper positioning of the substrate together with the π-π stacking interactions exerted by the Tyr^{243} side chain, although these last interactions are not catalytically indispensable (see below). This Tyr residue also hydrogen bonds through its hydroxyl group to the carboxyl oxygen of the reacting ester group, likely contributing to catalysis by stabilizing the negative charge developed at the phenoxide product upon nucleophilic attack of the catalytic Ser^{166}.

These results strongly suggest that medium-sized polyphenol derivatives such as digallates are ideal substrates for $TanB_{Fnn}$. As a consequence, the degradation of large TA derivatives by this enzyme is hypothesized to be progressive, in such a way that the digalloyl ester branches of tannins are initially recognized and sequentially cleaved by $TanB_{Fnn}$ to produce GA.

$TanB_{Fnn}$ binds spermidine

As described above, one of the protein molecules of the asymmetric unit of the $TanB_{Fnn}$ crystal showed a region

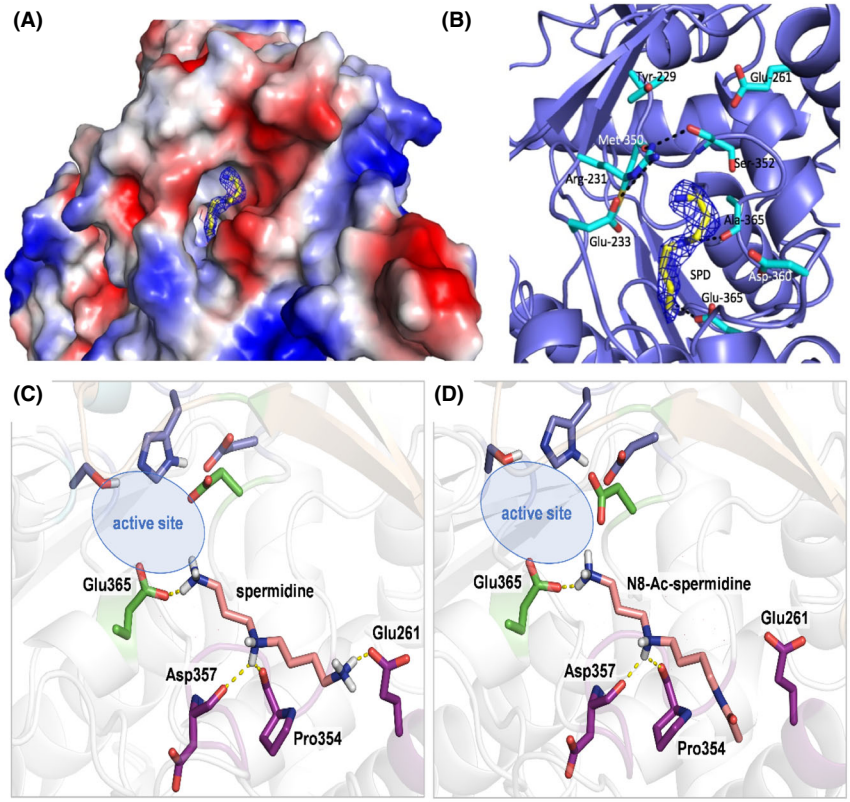

Fig. 5. Spermidine binding mode to $TanB_{Fnn}$.A. Spermidine (SPD; sticks model) is bound to $TanB_{Fnn}$ (shown as electrostatic potential molecular surface) in a cavity with an anionic entrance (red colour). SPD reaches the active site and directly interacts with the indispensable catalytic residue Glu^{365}. The *2Fo-Fc* electron density map (1σ level) is shown around the spermidine molecule.B. SPD-binding site in the same orientation as in (A) showing the amino acid side chains that decorate the entrance and walls of the cavity (shown as sticks model; see the text for details). Representative snapshots of 1 microsecond MD simulations of SPD (C) and N^8-acetylated SPD (D) (in red) bound to $TanB_{Fnn}$. Cationic polyamines accommodate in the rim located close to the enzyme active site by means of multiple hydrogen bonds mainly with negatively charged residues. Residues involved in binding, catalysis and located at the flexible lid are shown as green, blue and yellow sticks respectively. Non-polar hydrogens, solvent molecules and buffer ions have been omitted for clarity.

of elongated, well-defined electron density situated within the cavity of the enzyme that connects the active site with the bulk solvent (Fig. 5A). An exhaustive analysis of the environment around this density was found to be consistent with the presence of a spermidine (SPD) molecule. Binding of SPD to $TanB_{Fnn}$ in solution could also be inferred from the analysis of the effects of the polyamine on the thermal denaturation of the enzyme. This process was studied by recording the temperature dependence of the ratio of intrinsic tryptophan emission fluorescence of $TanB_{Fnn}$ at 350 and 330 nm, which as expected, increased upon thermal denaturation. Thermal unfolding of $TanB_{Fnn}$ fitted well to a two-state process with an apparent T_m value of 59.5 $\pm$ 0.1°C (Fig. S8A,B). When incubated with SPD (50 mM), the obtained T_m value decreased to 58.5 $\pm$ 0.1°C (Fig. S8C,D). The cavity of $TanB_{Fnn}$ that houses the SPD molecule shows an anionic character, which permits the accommodation of its positively charged amine groups. Three acidic residues decorate the entrance of the cavity (Glu^{233}, Glu^{261} and Asp^{360}), which would facilitate funnelling of SPD into the cavity interior (Fig. 5B). In this conformation, one of the terminal amine groups of SPD reaches the active site of $TanB_{Fnn}$ where it interacts with the carboxylate moiety of the catalytically essential residue Glu^{365}, whereas the most exposed one remains accessible to the solvent, close to the Glu^{233} side chain and to the positively charged Arg^{231} side chain (Fig. 5B). This latter cationic side chain is, however, highly oriented away from the cavity as a result of its participation in a complex array of interactions with Tyr^{229}, Ser^{352} and the main chain carbonyl oxygen of Met^{350}. Additionally, the N^4 nitrogen atom of SPD, situated in the centre of the cavity, is at hydrogen bond distance to the main chain carbonyl oxygen of Ala^{355} and also to a well-ordered water molecule. As a result of this binding mode, 87% of the complete surface area (296 $Å^2$ out of 340 $Å^2$) of SPD becomes buried in the $TanB_{Fnn}$ structure.

The structure and dynamics of the complexes between $TanB_{Fnn}$ and SPD or N^8-acetylated SPD were further analysed by molecular dynamics simulations starting from the crystallographic structure of the SPD-bound

enzyme. In all the performed simulations, SPD (Fig. 5C) and N^8-acetylated SPD (Fig. 5D) were observed to slightly slide away from the crystallographic binding pose, arriving at a densely negatively charged rim in which glutamic (Glu^{365}, Glu^{261}) and aspartic acid (Asp^{357}, Asp^{446}) residues accumulate. The N^1 and N^8 termini of SPD form persistent although highly dynamic salt bridges with these negative charges, and the central ammonium group also interacts with the backbone carbonyl of Pro^{354}. This type of binding mode involving the interaction of the central positive charge with neutral backbone carbonyl groups or water molecules has been observed in the crystallographic structures of *Plasmodium falciparum* (Sprenger *et al*., 2015) and *Synecochoccus* spermidine synthases (Guedez *et al*., 2019).

The densely charged polyammonium character and linear structure of these ligands was found to be critical for their recognition by $TanB_{Fnn}$. Also, the spacing between its positive charges seems to be nearly ideal in SPD, allowing it to interact with up to four polar residues (or even five) for the most part of the simulations. Interestingly, SPD was observed to tumble inside the interaction site in some simulations, alternatively exposing its N^1 and N^8 ammonium groups to the solvent. Both SPD and N^8-acetylated SPD exhibited a low residence time in their recognition site, quickly migrating to the bulk solvent after around 200 ns of simulation due to their very high hydrophilic character. The reduced hydrophilicity of N^8-acetylated SPD might be one of the causes for its superior inhibition properties with respect to SPD (see below).

Molecular modelling of polyamine binding to $TanB_{Fnn}$ infers the flexibility of the active site lid

Strikingly, a wide opening of the active site flap, which was not observed in the simulations of either the unliganded or substrate-bound states, was observed for the complexes with polyamines (Fig. 6A). Of note, high flexibility and plasticity was observed for this hairpin-like substructure, often returning to the closed state within the same simulation (Fig. 6B-E). This enhanced flexibility seems to be triggered by the presence of cationic polyamines near the negatively charged residues close to the binding/active site, likely by disrupting their polar interactions network either through direct contacts, long-range electrostatic perturbation or even by solvent inclusion. The observation of this type of motion involving a quite large (30 amino acids) and structured region of the protein in our microsecond molecular dynamics simulations was unexpected, since normally they occur in the millisecond timescale (Henzler-Wildman and Kern, 2007). Quite different amplitudes were observed for this motion, which strongly suggests that $TanB_{Fnn}$ is able to recognize and bind substrates of different sizes. This computational prediction agrees with the experimental observation that $TanB_{Fnn}$ is able to degrade small (methyl/ethyl gallate) to medium (epigallocatechin gallate) to very large (tannins) polyphenols.

Overall, these results suggest that, in addition to the expected blocking of the substrates access to the catalytic site, polyamines binding to $TanB_{Fnn}$ might also induce inhibition of the enzyme by altering the dynamics of the flexible lid and regulate the recognition of polyphenolic substrates.

Inhibition of $TanB_{Fnn}$ by polyamines affects F. nucleatum fitness

Different biochemical experiments were carried out in order to test the effects of SPD and its acetyl derivatives on the enzymatic activity of $TanB_{Fnn}$. Both SPD and its acetylated forms inhibited the activity of the enzyme against MG (Fig. 7A). Among the acetylated forms of SPD tested, N^8-acetyl SPD was the most effective inhibitor of the protein, completely abolishing hydrolytic activity at the highest concentration (50 mM).

The role of different $TanB_{Fnn}$ residues in SPD-induced activity inhibition was further studied based on the structural and molecular modelling data. As an initial approach, we tested the inhibitory capacity of SPD against the hydrolytic activity of $TanB_{Fnn}$ single point variants of residues located at the SPD-binding site. Interestingly, the protein variant $Phe^{234}Ala$ was almost insensitive to SPD inhibition (Fig 7B), suggesting that the $Phe^{234}Ala$ variant populates open states in solution at a greater extent than the wild-type enzyme.

As previously postulated, tannase activity might have an adaptative role for *F. nucleatum*, increasing the pathogen fitness in the presence of gallotannin compounds. Therefore, the inhibition of tannase activity by SPD and derivatives might also have implications for its survival. To further corroborate a putative role for spermidine on the regulation of bacterial susceptibility to diet phenolics, the maximum end-point growth capacity of *F. nucleatum* at subinhibitory concentrations was studied for MG, propyl gallate (PG) and TA in the presence and absence of SPD. Our results showed an impaired growth of *F. nucleatum* in the presence of all three compounds when SPD was present in the culture media (Fig. 7C). Similarly, the addition of SPD reduced the MICs (Fig. 7 D) and MBCs (Fig. 7E) of the compounds to impair the growth of *F. nucleatum* and kill the bacterium respectively. To further corroborate the effect of SPD on the degradative capacity of $TanB_{Fnn}$ in culture and its involvement in bacterial susceptibility to gallotannins, GA, the product of the reaction, was measured in the culture supernatant when MG was present in the culture

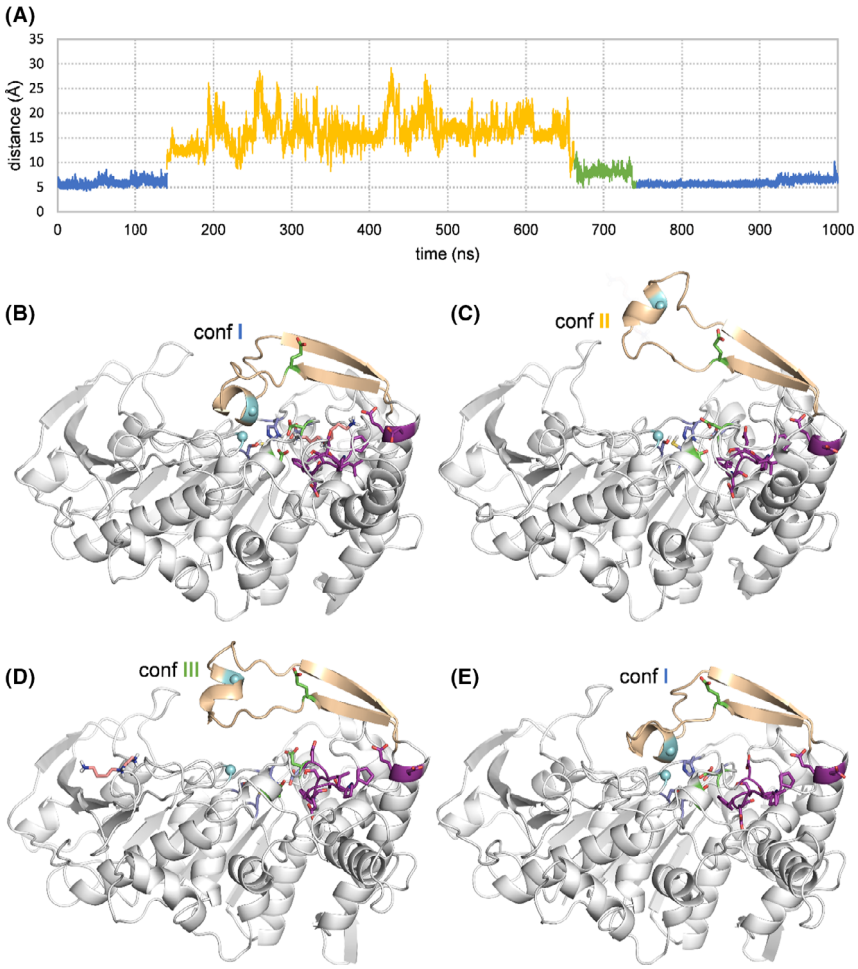

Fig. 6. Conformation of the flexible lid (in light brown) along a 1 microsecond MD simulation of spermidine bound to $TanB_{Fnn}$.A. By monitoring the distance between the Cα of residues Tyr^{239} and Gly^{77} located (shown as cyan spheres in the figures below), conformational transitions between closed (in blue), open (in yellow) and half-open (in green) arrangements of the flexible lid were observed throughout the simulation.B. Initially, when spermidine is bound in the active site, the lid is closed as observed in the X-ray structure (conf I, representative snapshot taken after 20 nanoseconds).C. After a while, spermidine abandons its interaction site and the lid opens widely for the most part of the simulation (conf II, representative snapshot taken after 207 nanoseconds).D. In the final part of the simulation, the amplitude of the lid opening is reduced (conf III, representative snapshot taken after 648 nanoseconds) and finally, (E) returns to the starting closed arrangement (conf I, representative snapshot taken after 763 nanoseconds). Residues involved in binding, catalysis and located at the flexible lid are shown as green, blue and yellow sticks respectively. Non-polar hydrogens, solvent molecules and buffer ions have been omitted for clarity.

media at subinhibitory concentrations. GA measurements were normalized to bacterial growth using OD measurements. SPD reduced the capacity of the bacteria to generate GA (Fig. 7F). As a whole, these results show that the action of SPD on $TanB_{Fnn}$ activity avoids the clearance of MG from the culture medium and results in increased levels of this compound in culture, which eventually affects negatively *F. nucleatum* survival and growth.

Discussion

The discovery of the role of *F. nucleatum* in the progression of some CRCs makes this oral bacterium a new target in order to control the disease. However, and despite the importance of the diet in the aetiology of colorectal malignancies, no information is available regarding the genetic determinants that regulate the interaction of the bacterium with food components in order to facilitate their survival and growth within the tumour environment. Recently, tannic acids have been demonstrated to be cytotoxic for a panel of CRC-derived cells lines, while their degradative product, pyrogallol, did not affect the growth of these cells (Oehmcke-Hecht *et al.*, 2020). Indeed, the presence of the opportunistic gut pathogen, *Streptococcus gallolyticus*, abrogated the cytotoxic capacity of tannic acids (Oehmcke-Hecht *et al.*, 2020). Increasing evidence indicates that oral pathobionts found in the gut during disorders such as CRC seem to originate from the oral niche through translocation

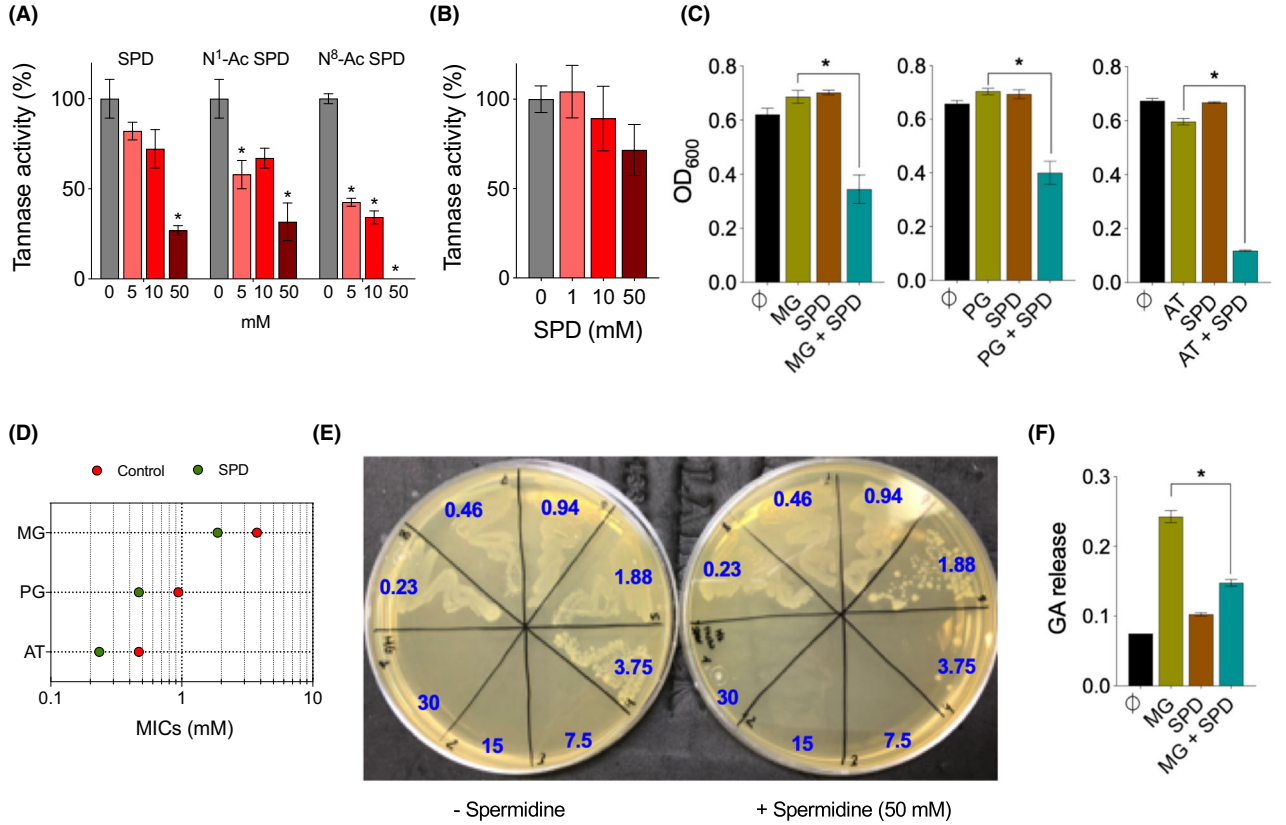

Fig. 7. Experimental inhibition of $TanB_{Fnn}$.A. Inhibition by spermidine (SPD) and acetyl derivatives of SPD of tannase activity over MG relative to control reactions without biogenic amines.B. Relative activity of the variant $Phe^{234}A$ $TanB_{Fnn}$ tannase in the absence and presence of different SPD concentrations.C. Maximum growth capacity measured as absorbance at 600 nm after 48 h of *F. nucleatum* subsp. *nucleatum* growth in its base medium (control) or in the presence of gallotannins (MG-Methyl gallate, PG-Propyl gallate, TA-Tannic acid) alone or in combination with 50 mM SPD. Minimum inhibitory (MIC) (D) and minimum bactericidal concentrations (MBCs) (E) of MG alone (left) or combined with SPD at 50 mM. The numbers in (E) represent the methyl gallate concentrations (mM) used.F. GA released from *F. nucelatum* subsp. *nucleatum* transformation of MG grown in its basal medium, the presence of 1 mM MG, 50 mM SPD or the combination of SPD and MG at the same concentrations. The experiments shown correspond to the average ± SE of 3–4 determinations and represent one of 2–3 performed. *Student's *t*-test, $P < 0.05$.

mechanisms to the gastrointestinal tract that are currently unknown (Flemer *et al.*, 2018; Schmidt *et al.*, 2019). The survival mechanisms of these pathogens might therefore be important for bacteria settlement, initially, in the mouth niche, in order to handle the continuous exposure to diet gallotannins and also for their increased fitness when they reach their gut destination. Homology with previously known tannases led us to identify a tannase enzyme that contributes to food metabolite detoxification as a survival advantage for *F. nucleatum* in the intestinal ecosystem.

To further understand the role of tannase activities in the mouth–gut adaptation of *F. nucleatum*, structural studies were performed with $TanB_{Fnn}$ which have identified new features of the flap covering the active site, with direct implications in the accessibility of substrates, and further, the existence of a polyamine binding site in $TanB_{Fnn}$. Notably, molecular dynamics simulations have also unveiled an unexpected role for SPD and its acetylated derivatives as modulators of the flap dynamics and consequently of enzymatic activity. SPD and some of its acetyl derivatives, particularly N^8-acetyl SPD, inhibit the hydrolytic activity of $TanB_{Fnn}$ against gallate derivatives revealing the existence of an *in vitro* interaction between the protein and the metabolites. This inhibitory activity has been confirmed using biochemical assays both with the purified protein and in microbial cultures, in which diet gallotannins result more toxic for the bacteria when polyamines are present due to an impaired detoxicant activity by $TanB_{Fnn}$. The reason for the differential ability of SPD and its acetylated derivatives is unclear. One possibility is that binding of SPD derivatives to the active/binding site takes place predominantly through two charged ammonium groups (the internal N4 and either the terminal N1 or N8, Fig. S9). In N1- and N8-acetyl SPD, one of the terminal groups is neutral due to

acetylation, which could make these derivatives less solvated (as this terminus would be quite solvent-exposed in our proposed binding models) and thus less prone to be detached from the active site. Related to this, the smaller desolvation penalty upon binding expected for N1- and N8-acetyl SPD (bearing two positive charges each) with respect to that of SPD (bearing three positive charges) would increase the binding affinity of the acetylated derivatives. On the other hand, the spacing between the two charged ammonium groups (three methylene groups in N8-Ac-SPD and four methylene groups in N1-Ac-SPD) would be the main factor contributing to the optimal recognition of N8-Acetyl SPD by the binding site residues.

The role of polyamines in cancer has been widely reported (Case ro *et al*., 2018). In particular, SPD and its acetylated derivatives have been postulated as protective molecules in cancer and age-related disorders (Madeo *et al*., 2018). The combined analysis of microbiota and metabolomics has shown increased *F. nucleatum* abundance as CRC progresses in a large cohort of patients (Yachida *et al*., 2019), while acetylated SPD levels significantly decrease with progression. Our results support at the molecular level the observed *F. nucleatum*-SPD inverse correlation. They suggest a mechanism by which the higher the level of SPD derivatives in faeces, the lower the detoxicant activity of $TanB_{Fnn}$, and, as a consequence, the fitness of the bacteria when diet gallotannins are present.

We previously described a tannase enzyme from a close relative to *F. nucleatum subs. nucleatum* (*F. nucleatum subs. polymorphum)*, $TanA_{Fnp}$ (Tomás-Cortázar *et al*., 2018). Both enzymes share a high degree of homology, especially at the regulatory flap and SPD-binding regions. Both enzymes differ in 35 residues out of 495 (93% sequence identity), with no differences situated in the flap, active site or polyamine binding site regions. Since both subspecies constitute pathogenic microorganisms, albeit with differential associations to disease, while exposed to gallotannins in both niches, it is plausible to hypothesize that similar mechanisms of detoxification are present in pathogenic fusobacteria, as a general survival strategy in these environments. In this regard, searches in public databases for tannases homologous to $TanB_{Fnn}$ within the order Fusobacteriales reveal the presence of these enzymes exclusively in the genera *Leptotrichia* and *Fusobacterium*. Multiple sequence alignments reveal that those from *Leptotrichia sps*. (sequence identities ranging from 40% to 58%) have much longer N-terminal segments (*L. wadei*), shorter flaps due to the lack of an $\alpha7$ helix region and finally, lack of the connecting loop formed by $\alpha13 - \alpha14$ (Fig. S10). Additionally, as described above, homologous tannases were also found in the bacterial genera that are predominant in the oral cavity: *Veillonella, Aggregatibacter, Selenomonas* and *Mitsuokella* (with overall sequence identities ranging from 40% to 50%). In these cases, the most variable regions also correspond to the putative flaps of the enzymes, while the connecting loop $\alpha13$-$\alpha14$ is not observed. Remarkably, larger putative flaps are present in the genera *Selenomonas, Veillonella* and *Mitsuokella* (Fig. S11), pointing to specific catalytic and/or regulatory features. These results indicate that tannases are distributed in bacterial genera present in the human oral cavity, most probably constituting part of the enzymatic toolkit of this environment. A similar analysis with bacterial genera of the human gut (Yachida *et al*., 2019) revealed putative tannases with sequence identities ranging from 43% to 60% (Fig. S12). We identified a high sequence variability in the equivalent flap regions and absence of segments similar to the $TanB_{Fnn}$ connecting loop $\alpha13$-$\alpha14$. Although the general trend in these species is the presence of shorter or absent flaps (*Lachnoclostridium*), larger putative flaps are also evident in some genera (*Megasphaera* and *Veillonella*). This structural variability suggests the presence of a large spectrum of α/β hydrolases in the human gut with a broad range of substrate specificities and regulatory characteristics.

Overall, our results describe the regulation of a microbial enzymatic activity by biogenic amines and identify a regulatory mechanism that affects a CRC-associated pathogen survival. These results also highlight the interplay between the presence of protective activities against deleterious food components for *F. nucleatum* and the presence of inhibitory molecules such as polyamines. This balance creates the opportunity to target therapeutically pathogen pro-survival activities and therefore prevent the initiation of pathogenic activities that could potentiate pro-tumoral responses.

Experimental procedures

Bacterial strains and culture conditions

Escherichia coli strains DH5α and BL21 (DE3) were used as transformation and expression hosts respectively. *Fusobacterium nucleatum subsp nucleatum Knorr 25586* was used for *$TanB_{Fnn}$* gene amplification. *F. nucleatum subs nucleatum Knorr 23726* was used in all the experiments. *E. coli* was grown in LB medium or LB medium containing ampicillin (100 $\mu g\ ml^{-1}$) and chloramphenicol (25 $\mu g\ ml^{-1}$) at 37°C with agitation. *F. nucleatum* was grown under anaerobic conditions in Tryptic Soy Broth (TSB) medium with 10% foetal bovine serum and 10% L-Cysteine. Details about phenolic degradation and inhibition experiments are explained bellow.

Computational analysis of the genes in the GADP pathway

To determine the abundance of tannase human orthologues, we took advantage of the web-tool MetaQuery (Nayfach *et al*., 2015), which allowed us to test its abundance in 10 different publicly available human gut metagenomes studies, including 2271 samples from 1962 subjects. Putative orthologues were detected at the phylum level via BLASTp against MetaQuery's own database with a minimum of > 30% amino acid identity, 70% Query and target coverage and a *P* value under 10^{-5} to account for orthologues in phylogenetic distant species. Additionally, the web-tool MetaPhlAn (Segata *et al*., 2012) allowed us to estimate the abundance of taxonomic groups and performed linear regression to identify taxa related to variations in the levels of tannase. Then functional group annotation was performed using the KEGG (Kanehisa and Goto, 2000) and eggNOG (Powell *et al*., 2012) databases. Reference gene annotations were retrieved from the GigaScience database (Li *et al*., 2014). MetaQuery also implements Wilcoxon rank-sum tests to identify genes, functions and taxa appearing as differentially abundant between cases and controls.

Gene cloning

Genomic DNA from *F. nucleatum* subsp. *nucleatum 25586* was isolated using a previously described bacteria DNA isolation protocol (Tomás-Cortázar *et al*., 2018). Standard molecular biology procedures were followed to clone the tannase gene avoiding the signal peptide of the protein. The gene was PCR-amplified from genomic DNA using Phusion Hot Start II polymerase (Thermo Fisher Scientific, Waltham, MA, USA) with primers *TanB$_{Fnn}$* Forward and *TanB$_{Fnn}$* Reverse. The PCR product was purified using a PCR purification kit (Thermo Fisher Scientific). The 1.5 kb PCR product and the vector pHis parallel 2 (Addgene) were digested with *Nco*I and *Sal*I and then ligated for 16 h using T4 DNA ligase (Promega, Madison, WI, USA). The ligation mixture was transformed into DH5α cells, and positive colonies were verified by colony PCR and sequencing. Positive plasmids (pHIS parallels II-*TanB$_{Fnn}$*) were finally transformed into *Escherichia coli* BL21 (DE3) cells for protein production.

Protein production and purification

Sequence-confirmed *TanB$_{Fnn}$*-containing plasmids were transformed into *E. coli* BL21 (DE3). The bacteria were then grown in Luria–Bertani medium (Pronadisa) supplemented with Ampicillin and induced with 1 mM IPTG for 16 h at 20°C. The His-tag fusion protein was then purified by nickel affinity chromatography (GE Healthcare, Uppsala, Sweden) and eluted in 20 mM Tris (VWR, V-0497), pH 7.5, 150 mM NaCl (Thermo Fisher Scientific, S0520) and 250 mM Imidazole. Eluted fractions containing TanB$_{Fnn}$ were identified by SDS-PAGE, pooled, concentrated and loaded onto a HiLoad 10/300 GL Superdex 75 column (GE Healthcare) pre-equilibrated in 20 mM Tris pH 7.5, 150 mM NaCl (Thermo Fisher Scientific, S0520), using an AKTA chromatography system (GE Healthcare). Fractions containing TanB$_{Fnn}$ were confirmed by SDS-PAGE, pooled, concentrated and stored at −80°C until used. Protein concentration was determined using the BCA protein assay kit (Thermo Fisher Scientific).

Determination of tannase activity

The generation of gallic acid in hydrolysis reactions was determined in triplicate with the following assay: TanB$_{Fnn}$ (1 μg) in 100 μL of 50 mM phosphate buffer, pH 6.5, was incubated with 100 μl of 25 mM methyl gallate (1 mM final concentration) for 10 min at 37°C. After incubation, 150 μl of a methanolic rhodanine solution (0.667% rhodanine in 100% methanol) was added to the reaction mixture. After 5 min of incubation at 30 °C, 100 μl of 0.5 M KOH (Sigma Aldrich, 1050121000) plus 900 μl of water were added and the absorbance at 520 nm was measured on a spectrophotometer. A standard curve using gallic acid concentrations ranging from 0.125 to 1 mM was prepared. One unit of tannase activity was defined as the amount of enzyme required to release 1 μmol of gallic acid per minute under standard reaction conditions.

Inhibition assays with SPD and derivatives were performed as indicated above with an additional step including a pre-incubation of the enzyme (Room temperature) for 30 min with the inhibitor before the addition of methyl gallate.

Biochemical characterization

TanB$_{Fnn}$ activity was measured at 4, 22, 30, 37, 45, 55 and 65 °C to determine the optimal temperature for enzymatic activity. The optimum pH value for tannase activity was determined by studying its pH dependence within the pH range between 3 and 10. The buffers used were the following: acetic acid–sodium acetate buffer for pH 3–5, citric acid–sodium citrate for pH 6, sodium phosphate for pH 7, Tris–HCl for pH 8, glycine–NaOH for pH 9 and sodium carbonate–bicarbonate for pH 10. A 100 mM concentration was used for all buffers. The rhodanine assay was used for the optimal pH characterization of TanB$_{Fnn}$ (Jimenez *et al*., 2014a). Since the rhodanine–gallic acid complex forms only under basic conditions, after the enzymatic degradation of methyl gallate, 100 μl of 0.5 M KOH was added to the reaction

mixture to ensure that the same pH value (pH 11) was achieved in all samples assayed.

For temperature stability measurements, $TanB_{Fnn}$ was incubated in 50 mM phosphate buffer, pH 6.5, at 22, 30, 37, 45, 55 and 65 °C for 30 min and 1, 2 and 18 h. After incubation, the residual activity was measured as described above.

$TanB_{Fnn}$ substrate specificity

The activity of $TanB_{Fnn}$ against 27 potential substrates was analysed. The substrates assayed were gallic esters (methyl gallate, ethyl gallate, propyl gallate, and lauryl gallate), benzoic esters (methyl benzoate and ethyl benzoate), hydroxybenzoic esters (methyl 4-hydroxybenzoate, ethyl 4-hydroxybenzoate, propyl 4-hydroxybenzoate and butyl 4-hydroxybenzoate), a vanillic ester (methyl vanillate), dihydroxybenzoic esters (methyl 2,4-dihydroxybenzoate, ethyl 3,4-dihydroxybenzoate or protocatechuic acid ethyl ester and ethyl 3,5-dihydroxybenzoate), a gentisic ester (methyl gentisate), a salicylic ester (methyl salicylate) and ferulic esters (ferulic methyl ester and ferulic ethyl ester). Tannic acid and epigallocatechin gallate were also assayed as potential substrates. Recombinant $TanB_{Fnn}$ (10 μg ml^{-1}) was incubated at 37°C in ammonium acetate 50 mM, pH 5 in the presence of the substrate (1 mM). As controls, acetate buffers containing the reagents but not the enzyme were incubated under the same conditions. After incubation, the samples were analysed by high-performance liquid chromatography with diode array detection (HPLC–-DAD). A Thermo chromatograph (Thermo Fisher Scientific) equipped with a P4000 SpectraSystem pump, an AS3000 autosampler and a UV6000LP photodiode array detector was used. A gradient of solvent A (water–acetic acid, 98:2 [vol/vol]) and solvent B (water–acetonitrile–-acetic acid, 78:20:2 [vol/vol/vol]) was applied to a reversed-phase Nova-pack C18 cartridge (25 cm by 4.0-mm inside diameter [i.d.]; 4.6-μm particle size) at room temperature as follows: 0–55 min, 80% B linear, 1.1 ml min^{-1}; 55–57 min, 90% B linear, 1.2 ml min^{-1}; 57–70 min, 90% B isocratic, 1.2 ml min^{-1}; 70–80 min, 95% B linear, 1.2 ml min^{-1}; 80–90 min, 100% linear, 1.2 ml min^{-1}; 100–120 min, washing, 1.0 ml min^{-1}; and re-equilibration of the column under the initial gradient conditions. Samples were injected onto the cartridge after being filtered through a 0.45-μm PVDF filter. Detection of the substrates and the degradation compounds was performed spectrophotometrically by scanning from 220 to 380 nm. The identification of degradation compounds was carried out by comparing the retention times and spectral data of each peak with those of standards from commercial suppliers.

Gallotannins degradative capacity of *F. nucleatum*

A bacterial pre-inoculum was initially grown to exponential phase without phenolic compounds. From this inoculum, *F. nucleatum* was diluted to an optical density (OD) of 0.1 in tubes with either 1 mM Methyl gallate, Ethyl Gallate or Tannic acid. Tubes containing medium without any compound and medium containing phenolic compounds but without *F. nucleatum* were also included as controls. Cultures were grown in the dark under anaerobic conditions for one week. After one week, supernatants were collected and gallotannin transformation was analysed using high-performance liquid chromatography with diode array detection (HPLC–DAD) as described above.

Minimum inhibitory and bactericidal concentration determination

The minimum inhibitory concentrations (MICs) were determined by a broth microdilution assay. Briefly, in a 96-well plate, serial double dilutions of the compounds (from 30 to 0.23 mM) were prepared using fresh TSB complemented broth. The inoculum was adjusted in order to obtain a final optical density of 0.05 at 600 nm in each well, and it was loaded in a final volume of 200 μl. After an incubation at 37°C for 48 h under anaerobic conditions, bacterial growth was recorded visually, and the MIC was determined as the lowest concentration of the phenolic compound at which the visible growth was inhibited. To confirm each MIC and establish the minimum bactericidal concentration (MBC), 5 μl of each well showing no growth was inoculated in compound-free agar plates and incubated at 37°C for 48 h. The MBC values were determined as the lowest concentration that prevented the growth of the bacteria. When combined inhibition of phenolics with spermidine was tested, 50 mM spermidine was added in the media with all the phenolic compounds concentrations tested. Control wells with spermidine and without phenolic compound were also seeded to discard spermidine effects on growth.

Controls were included in all cases. For the MIC determination, inoculated and uninoculated wells of compound-free broth were used to control the adequacy of the broth and to guarantee the sterility of the experiment respectively. Also, serial double dilutions of 96% EtOH were added to evaluate the effect of the alcohol in the growth of the bacteria. For the MBC determination, a positive control was used in all the cases to check and guarantee the optimal growth conditions of the bacteria in the agar plate. All of the experiments were performed independently at least four times. The maximum growth

of *F. nucleatum* was evaluated at subinhibitory concentrations of the phenolic compounds. The optical density was recorded after 48 h at 600 nm. As controls, inoculated and uninoculated wells of phenolic-free broth, as well as uninoculated wells with the phenolic compounds, were used. At least three independent experiments were performed with 3 replicates each.

Transcriptional response of *F. nucleatum* to tannic acid

To determine the transcriptional response to TA, *F. nucleatum subsp. nucleatum* cultures (12 ml each) were grown in complemented TSB lacking TA to an $OD_{600} \approx 0.5–0.7$. The cultures were then induced with TA for 10 min at a final concentration to 0.1 mM. Control cultures with no added TA were processed identically in parallel. Total RNA was extracted from the bacterial pellets quenched with RNAprotect Bacteria Reagent (Qiagen, Barcelona, Spain) using the Direct-Zol RNA miniprep Plus kit (Zymo Research, Irvine, CA, USA), after lysis in TRIzol (Thermo Fisher Scientific) using a FastPrep-24 5G Homogenizer (1 cycle of 45s at 6.5 m/s speed, MP bio). The quantity and quality of the RNAs were evaluated using a NanoDrop ND-1000.

RNA was reverse-transcribed using M-MLV reverse transcriptase (Thermo Fisher Scientific). Real-time PCR was then performed using the SYBR Green PCR Master Mix (PerfeCTa® SYBR® Green SuperMix, Low ROX™, Quanta Biosciences) on a QuantStudio™ 6 Real-Time PCR System (Thermo Fisher Scientific). Fold induction of the genes was calculated relative to 16s rRNA using the $2^{-\Delta\Delta C_t}$ method. The primers used are listed in Table 2.

Table 2. Primers used

Target	Oligonucleotide sequence
Cloning	
TanB$_{Fnn}$-F	5'-CGC CAT GGG CAT GGT AAA AAA TG-3'
TanB$_{Fnn}$-R	5'-CGC GGT CGA CTT ATT TTT TTA CAA C-3'
Asp^{150}Ala-F	5'-TAG ATA TCT ATA TCT TAA TGC TGA AGT TAT GCC AGG AGA T-3'
Asp^{150}Ala-R	5'-ATC TCC TGG CAT AAC TTC AGC ATT AAG ATA TAG ATA TCT A-3'
Ser^{166}Ala-F	5'-ATA ATT TCA AAT GGG ACA GCT GCT GGT GGT GCA TTA TCT-3'
Ser^{166}Ala-R	5'-AGA TAA TGC ACC ACC AGC AGC TGT CCC ATT TGA AAT TAT-3'
Phe^{234}Ala-F	5'-AAT TCA TAT TCA AGA ATG GAA GCT ACT AGA AAT ACT TCT GCT CAA GAA-3'
Phe^{234}Ala-R	5'-TTC TTG AGC AGA AGT ATT TCT AGT AGC TTC CAT TCT TGA ATA TGA ATT-3'
Tyr^{243}Ala-F	5'-GAA ATA CTT CTG CTC AAG AAG CTA ACG ATA GAA GTT TAA CTC GTT CAA C-3'
Tyr^{243}Ala-R	5'-GTT GAA CGA GTT AAA CTT CTA TCG TTA GCT TCT TGA GCA GAA GTA TTT C-3'
Asn^{244}Ala-F	5'-GAA ATA CTT CTG CTC AAG AAT ATG CTG ATA GAA GTT TAA CTC GTT CAA C-3'
Asn^{244}Ala-R	5'-GTT GAA CGA GTT AAA CTT CTA TCA GCA TAT TCT TGA GCA GAA GTA TTT C-3'
Arg^{246}Ala-F	5'-GCT CAA GAA TAT AAC GAT GCT AGT TTA ACT CGT TCA ACT-3'
Arg^{246}Ala-R	5'-AGT TGA ACG AGT TAA ACT AGC ATC GTT ATA TTC TTG AGC-3'
Real-time PCR	
TanB$_{Fnn}$-F	5'-TGGAGAATAAGACATGGAGCAG-3'
TanB$_{Fnn}$-R	5'-CCCAAGGAGAAGCAAAGTCT-3'
16S rRNA-F	5'-CTTAGGAATGAGACAGAGATG-3'
16S rRNA-R	5'-TGATGGTAACATACGAAAGG-3'

Protein mutagenesis

Single point TanB$_{Fnn}$ mutants were constructed by a site-directed mutagenesis PCR using the plasmid pHIS parallels II-*TanB*$_{Fnn}$ as template. The mutagenic primers used to introduce the amino acid changes are described in primers Table. PCR-like products were then digested with *Dpn*I and transformed into *E. coli* as previously described. The mutated *TanB*$_{Fnn}$ genes were sequenced to verify the expected nucleotide changes.

X-ray crystallography

Initial crystallization conditions for TanB$_{Fnn}$ were performed by the sitting-drop vapour diffusion method at 291 K using commercial screenings from Hampton Research (Riverside, CA, USA) and Qiagen in Innovaplate SD-2 96-well plates set up using an Innovadyne Nanodrop robot. Each drop consisted of 250 nl protein solution (10 mg ml^{-1}) in Tris–HCl buffer (20 mM Tris–HCl pH 8.0 containing 0.1 M NaCl) and 250 nl reservoir solution. Drops were equilibrated against 65 μl reservoir solution. Crystals were observed in 25% (*w/v*) PEG 3350, 0.1 M Tris–HCl pH 8.5 and in 25% (*w/v*) PEG 3350, 0.1 M Hepes, pH 7.5. Scaling up and optimization of the crystallization conditions using hanging drops in 24-well VDX plates required the removal of the *N*-terminal His-tag by proteolytic treatment with TEV endoprotease (Angulo *et al.*, 2011). The best crystals were finally obtained in 25% (*w/v*) PEG 3350, 0.1 M Tris–HCl pH 8.5 (1:1 protein:precipitant volume ratio; total volume 2 μl). Crystals were cryoprotected in the precipitant solution supplemented with 20% (*v/v*) glycerol prior to flash cooling at 100 K. Diffraction data were collected in the BL-13 XALOC beamline at the ALBA synchrotron (CELLS-ALBA, Spain), using a Pilatus 6M detector (Area Detector Systems Corp.) and a wavelength of 0.97926 Å. The best data set consisting of 2400 images taken with a 0.15° oscillation angle and a crystal-to-detector distance of 368.08 mm was processed with *XDS* (Kabsch, 2010) and Aimless (Evans and Murshudov, 2013). Crystals diffracted up to 2.4 Å resolution and belonged to the

monoclinic space group P 2_1 with unit cell dimensions of $a = 71.84$, $b = 91.07$, $c = 124.07$ Å, $b = 101.696°$. Three $TanB_{Fnn}$ molecules were found in the asymmetric unit yielding Matthews coefficient of 2.28 $Å^3$/Da. The structure of $TanB_{Fnn}$ was solved by molecular replacement using *Phaser* (McCoy *et al*., 2007). Refinement and manual model building were performed with Phenix (Adams *et al*., 2010) and Coot (Emsley *et al*., 2010) respectively. The stereochemistry of the final model was checked with MolProbity (Chen *et al*., 2010). The final model of the structure included all residues of the polypeptide chain (495 amino acids) except the four N-terminal residues, the C-terminal residue Lys^{495} and the segment comprising residues Arg^{396} to Ile^{407}. The $2F_o$-F_c electron density map showed continuous density for the rest of the protein, although some exposed side chains from residues situated in the connecting loops β1-β2 (Asn^{23} and Lys^{25}) and α7-β11 (Thr^{249} and Arg^{250}) were not well defined in the electron density map. Data collection and processing statistics are shown in Table 1. Figures of protein models were prepared with PyMOL (The PyMOL Molecular Graphics System, version 2.0. Schrödinger, LLC, Mannheim, Germany).

Thermal denaturation determination

Thermal denaturation assays were performed with a Tycho NT 6.0 (Nanotemper technologies, Munich). Protein thermal unfolding was studied by measuring the ratio of the intrinsic tryptophan fluorescence at 350 and 330 nm upon excitation at 295 nm. The change in the signal ratio was monitored from 35 to 95°C. Analysis of the thermal curves was performed using the software of the instrument. Protein concentration was 0.2 mg ml^{-1} in the absence or presence of 50 mM spermidine.

Molecular dynamics (MD) simulations

A nearly full-length model of $TanB_{Fnn}$ was obtained by homology modelling using Schrödinger Suite and the X-ray structure determined in this work as a template, thus reconstructing the unresolved flexible loop between residues Tyr^{394} and Ile^{409}. Catalytic His^{476} was modelled in its N-δ tautomeric form to preserve the integrity of the catalytic triad. Simulations were run both in the presence and absence of the Mg^{2+} crystallographically determined to be bound to residues Asp^{150} and Glu^{151}, without observing noticeable differences in the dynamic behaviour of both types of protein complexes. Unconstrained MD simulations in water were performed using the GPU accelerated code (*pmemd*) (Gotz *et al*., 2012; Pierce *et al*., 2012; Le Grand *et al*., 2013) of the Amber 18 and AmberTools 19 packages (Case *et al*., 2005). Parameters for ethyl gallate, spermidine and N8-acetylated spermidine were generated within the *antechamber* module using the upgraded version of the general Amber force field (*gaff2*) (Wang *et al*., 2004), with partial charges set to fit the electrostatic potential generated at the HF/6-31 G(d) level by the RESP (restrained electrostatic potential) model (Bayly *et al*., 1993). The charges were calculated according to the Merz–Singh–Kollman scheme (Besler *et al*., 1990; Singh and Kollman, 1984) using the Gaussian 16 package (Frisch et al., 2016). Each protein complex was immersed in a pre-equilibrated cubic box with a 10 Å buffer of TIP3P water molecules using the *leap* module, resulting in the addition of around 20 000 solvent molecules. The systems were neutralized by addition of explicit counter ions (Na^+ and Cl^-). All subsequent calculations were done using an evolved version of the Stony Brook modification of the Amber 99 force field (*ff14SB*) (Maier *et al*., 2015). A two-stage geometry optimization approach was performed. The first stage minimizes the positions of solvent molecules and ions imposing positional restraints on solute by a harmonic potential with a force constant of 500 kcal mol^{-1} $Å^{-2}$, and the second stage was a minimization of all the atoms in the simulation cell. The systems were gently heated under periodic boundary conditions at a constant pressure of 1 atm. Water molecules were treated with the SHAKE algorithm such that the angle between the hydrogen atoms was kept fixed. Long-range electrostatic effects were modelled using the particle mesh Ewald method (Darden *et al*., 1993). An 8 Å cut-off was applied to Lennard–Jones and electrostatic interactions. Harmonic restraints of 10 kcal mol^{-1} were applied to the solute, and the Andersen equilibration scheme was used to control and equalize the temperature. The time step was kept at 1 fs during the heating stage, allowing potential inhomogeneities to self-adjust for 100 ps. Each system was then equilibrated for 2 ns with a 2 fs time step at a constant volume and temperature of 300 K. Production trajectories were run for 1.0 μs under the same conditions.

Statistical analysis

The results are presented as means ± SE (standard error). Significant differences between means were calculated with Student's *t*-test. Multiple comparisons were analysed by ANOVA, followed by pairwise comparisons. A P value < 0.05 was considered significant. All statistical calculations were performed with GraphPad Prism ver. 8 (Graphpad Software, San Diego, CA, USA).

Conflicts of interest

The authors declare that they have no conflicts of interest related to this work.

References

Adams, P.D., Afonine, P.V., Bunkoczi, G., Chen, V.B., Davis, I.W., Echols, N., *et al*. (2010) PHENIX: a comprehensive Python-based system for macromolecular structure solution. *Acta Crystallographica Section D-Biological Crystallography* **66:** 213–221.

Alvarez, Y., Esteban-Torres, M., Cortes-Cabrera, A., Gago, F., Acebron, I., Benavente, R., *et al*. (2014) Esterase LpEst1 from *Lactobacillus plantarum*: a novel and atypical member of the alpha beta hydrolase superfamily of enzymes. *PLoS One* **9:** e92257.

Angulo, I., Acebron, I., de las Rivas, B., Munoz, R., Rodriguez-Crespo, I., Menendez, M. *et al*. (2011) High-resolution structural insights on the sugar-recognition and fusion tag properties of a versatile beta-trefoil lectin domain from the mushroom *Laetiporus sulphureus*. *Glycobiology* **21:** 1349–1361.

Barbieri, R., Coppo, E., Marchese, A., Daglia, M., Sobarzo-Sanchez, E., Nabavi, S.F., and Nabavi, S.M. (2017) Phytochemicals for human disease: an update on plant-derived compounds antibacterial activity. *Microbiol Res* **196:** 44–68.

Bayly, C. I., Cieplak, P., Cornell, W.D., and Kollman, P.A. (1993) A well-behaved electrostatic potential based method using charge restraints for deriving atomic charges: the RESP model. *J Phys Chem* **97:** 10269–10280.

Besler, B.H., Merz, K.M. Jr, and Kollman, P.A. (1990) Atomic charges derived from semiempirical methods. *J Comput Chem* **11:** 431–439.

Brennan, C.A., and Garrett, W.S. (2019) *Fusobacterium nucleatum* - symbiont, opportunist and oncobacterium. *Nat Rev Microbiol* **17:** 156–166.

Bullman, S., Pedamallu, C.S., Sicinska, E., Clancy, T.E., Zhang, X., Cai, D., *et al*. (2017) Analysis of *Fusobacterium* persistence and antibiotic response in colorectal cancer. *Science* **358:** 1443–1448.

Buzzini, P., Arapitsas, P., Goretti, M., Branda, E., Turchetti, B., Pinelli, P., *et al*. (2008) Antimicrobial and antiviral activity of hydrolysable tannins. *Mini Rev Med Chem* **8:** 1179–1187.

Case, D.A., Cheatham, T.E. 3rd, Darden, T., Gohlke, H., Luo, R., Merz, K.M. Jr, *et al*. (2005) The Amber biomolecular simulation programs. *J Comput Chem* **26:** 1668–1688.

Casero, R.A. Jr, Murray Stewart, T., and Pegg, A.E. (2018) Polyamine metabolism and cancer: treatments, challenges and opportunities. *Nat Rev Cancer* **18:** 681–695.

Chen, V.B., Arendall, W.B. 3rd, Headd, J.J., Keedy, D.A., Immormino, R.M., Kapral, G.J., *et al*. (2010) MolProbity: all-atom structure validation for macromolecular crystallography. *Acta Crystallogr D Biol Crystallogr* **66:** 12–21.

Darden, T., York, D., and Pedersen, L. (1993) Particle mesh Ewald: An N log(N) method for Ewald sums in large systems. *J Chem Phys* **98:** 10089.

Emsley, P., Lohkamp, B., Scott, W.G., and Cowtan, K. (2010) Features and development of Coot. *Acta Crystallogr D Biol Crystallogr* **66:** 486–501.

Evans, P.R., and Murshudov, G.N. (2013) How good are my data and what is the resolution? *Acta Crystallogr D Biol Crystallogr* **69:** 1204–1214.

Feng, Q., Liang, S., Jia, H., Stadlmayr, A., Tang, L., Lan, Z., *et al*. (2015) Gut microbiome development along the colorectal adenoma-carcinoma sequence. *Nat Commun* **6:** 6528.

Flemer, B., Warren, R.D., Barrett, M.P., Cisek, K., Das, A., Jeffery, I.B., *et al*. (2018) The oral microbiota in colorectal cancer is distinctive and predictive. *Gut* **67:** 1454–1463.

Flynn, K.J., Baxter, N.T., and Schloss, P.D. (2016) Metabolic and community synergy of oral bacteria in colorectal cancer. *mSphere* **1:** e00102-16.

Frisch, M. J., Trucks, G. W., Schlegel, H. B., Scuseria, G. E., Robb, M. A., Cheeseman, J. R., et al. (2016). *Gaussian 16 Rev. C.01*. Wallingford, CT: Gaussian, Inc.

Gotz, A.W., Williamson, M.J., Xu, D., Poole, D., Le Grand, S., and Walker, R.C. (2012) Routine microsecond molecular dynamics simulations with AMBER on GPUs. 1. *Generalized Born J Chem Theory Comput* **8:** 1542–1555.

Le Grand, S., Gotz, A.W., and Walker, R.C. (2013) SPFP: Speed without compromise-A mixed precission model for GPU accelerated molecular dynamics simulations. *Comput Phys Commun* **184:** 374–380.

Guedez, G., Pothipongsa, A., Siren, S., Liljeblad, A., Jantaro, S., Incharoensakdi, A., and Salminen, T. A. (2019) Crystal structure of dimeric *Synechococcus spermidine* synthase with bound polyamine substrate and product. *Biochem J* **476:** 1009–1020.

Haslam, E., and Stangroom, J. E. (1966) The esterase and depsidase activities of tannase. *Biochem J* **99:** 28–31.

Hemila, H., Koivula, T.T., and Palva, I. (1994) Hormone-sensitive lipase is closely related to several bacterial proteins, and distantly related to acetylcholinesterase and lipoprotein lipase: identification of a superfamily of esterases and lipases. *Biochim Biophys Acta* **1210:** 249–253.

Henzler-Wildman, K., and Kern, D. (2007) Dynamic personalities of proteins. *Nature* **450:** 964–972.

Holm, L., and Rosenstrom, P. (2010) Dali server: conservation mapping in 3D. *Nucleic Acids Res* **38:** W545–549.

Jimenez, N., Esteban-Torres, M., Mancheno, J. M., de Las Rivas, B., and Munoz, R. (2014a) Tannin degradation by a novel tannase enzyme present in some *Lactobacillus plantarum* strains. *Appl Environ Microbiol* **80:** 2991–2997.

Jimenez, N. S. L., Esteban-Torres, M., de las Rivas, B., Muñoz, R. (2014) Contribution of a tannase from *Atopobium parvulum* DSM 20469T in the oral processing of food tannins. *Food Res Int* **62:** 397–402.

Jimenez, N., Reveron, I., Esteban-Torres, M., Lopez de Felipe, F., de Las Rivas, B., and Munoz, R. (2014b) Genetic and biochemical approaches towards unravelling the degradation of gallotannins by *Streptococcus gallolyticus*. *Microb Cell Fact* **13:** 154.

Kabsch, W. (2010) *Xds. Acta Crystallogr D Biol Crystallogr* **66:** 125–132.

Kanehisa, M., and Goto, S. (2000) KEGG: kyoto encyclopedia of genes and genomes. *Nucleic Acids Res* **28:** 27–30.

Kolodzeij, H., Kayser, O., Latte, K.P., and Ferreira, D. (1999) Evaluation of the antimicrobial potency of tannins and related compounds using the microdilution broth method. *Planta Med* **65:** 444–446.

Kostic, A.D, Chun, E., Robertson, L., Glickman, J.N, Gallini, C.A., Michaud, M., *et al*. (2013) *Fusobacterium nucleatum*

potentiates intestinal tumorigenesis and modulates the tumor-immune microenvironment. *Cell Host Microbe* **14:** 207–215.

Krissinel, E., and Henrick, K. (2007) Inference of macromolecular assemblies from crystalline state. *J Mol Biol* **372:** 774–797.

de Las Rivas, B., Rodriguez, H., Anguita, J., and Munoz, R. (2019) Bacterial tannases: classification and biochemical properties. *Appl Microbiol Biotechnol* **103:** 603–623.

Li, J., Jia, H., Cai, X., Zhong, H., Feng, Q., Sunagawa, S., *et al*. (2014) An integrated catalog of reference genes in the human gut microbiome. *Nat Biotechnol* **32:** 834–841.

Liu, Y., Baba, Y., Ishimoto, T., Iwatsuki, M., Hiyoshi, Y., Miyamoto, Y., *et al*. (2019) Progress in characterizing the linkage between *Fusobacterium nucleatum* and gastrointestinal cancer. *J Gastroenterol* **54:** 33–41.

Lopez de Felipe, F., de Las Rivas, B., and Munoz, R. (2014) Bioactive compounds produced by gut microbial tannase: implications for colorectal cancer development. *Front Microbiol* **5:** 684.

Madeo, F., Eisenberg, T., Pietrocola, F., and Kroemer, G. (2018) Spermidine in health and disease. *Science* **359.**

Maier, J.A., Martinez, C., Kasavajhala, K., Wickstrom, L., Hauser, K.E., and Simmerling, C. (2015) ff14SB: improving the accuracy of protein side chain and backbone parameters from ff99SB. *J Chem Theory Comput* **11:** 3696–3713.

Matoba, Y., Tanaka, N., Noda, M., Higashikawa, F., Kumagai, T., and Sugiyama, M. (2013) Crystallographic and mutational analyses of tannase from Lactobacillus plantarum. *Proteins* **81:** 2052–2058.

McCoy, A.J., Grosse-Kunstleve, R.W., Adams, P.D., Winn, M.D., Storoni, L.C., and Read, R.J. (2007) Phaser crystallographic software. *J Appl Crystallogr* **40:** 658–674.

Mehta, R.S., Nishihara, R., Cao, Y., Song, M., Mima, K., Qian, Z.R., *et al*. (2017) Association of dietary patterns with risk of colorectal cancer subtypes classified by fusobacterium nucleatum in tumor tissue. *JAMA Oncol* **3:** 921–927.

Mima, K., Nishihara, R., Qian, Z.R., Cao, Y., Sukawa, Y., Nowak, J.A., *et al*. (2016) *Fusobacterium nucleatum* in colorectal carcinoma tissue and patient prognosis. *Gut* **65:** 1973–1980.

Nardini, M., and Dijkstra, B.W. (1999) a/b hydrolase fold enzymes: the family keeps growing. *Curr Opin Struct Biol* **9:** 732–737.

Nayfach, S., Fischbach, M.A., and Pollard, K.S. (2015) MetaQuery: a web server for rapid annotation and quantitative analysis of specific genes in the human gut microbiome. *Bioinformatics* **31:** 3368–3370.

Noguchi, N., Ohashi, T., Shiratori, T., Narui, K., Hagiwara, T., Ko, M., *et al*. (2007) Association of tannase-producing *Staphylococcus lugdunensis* with colon cancer and characterization of a novel tannase gene. *J Gastroenterol* **42:** 346–351.

Oehmcke-Hecht, S., Mandl, V., Naatz, L. T., Duhring, L., Kohler, J., Kreikemeyer, B., and Maletzki, C. (2020) *Streptococcus gallolyticus* abrogates anti-carcinogenic properties of tannic acid on low-passage colorectal carcinomas. *Sci Rep* **10:** 4714.

Ollis, D. L., Cheah, E., Cygler, M., Dijkstra, B., Frolow, F., Franken, S.M., *et al*. (1992) The a/b hydrolase fold. *Protein Eng* **5:** 197–211.

Pierce, L.C.T., Salomon-Ferrer, R., Augusto, F., de Oliveira, C., McCammon, J.A., and Walker, R.C. (2012) Routine access to millisecond time scale events with accelerated molecular dynamics. *J Chem Theory Comput* **8:** 2997–3002.

Powell, S., Szklarczyk, D., Trachana, K., Roth, A., Kuhn, M., Muller, J., *et al*. (2012) eggNOG v3.0: orthologous groups covering 1133 organisms at 41 different taxonomic ranges. *Nucleic Acids Res* **40:** D284–289.

Redondo, L.M., Chacana, P.A., Dominguez, J.E., and Fernandez Miyakawa, M.E. (2014) Perspectives in the use of tannins as alternative to antimicrobial growth promoter factors in poultry. *Front Microbiol* **5:** 118.

Ren, B., Wu, M., Wang, Q., Peng, X., Wen, H., McKinstry, W.J., and Chen, Q. (2013) Crystal structure of tannase from *Lactobacillus plantarum*. *J Mol Biol* **425:** 2737–2751.

Reveron, I., Rodriguez, H., Campos, G., Curiel, J.A., Ascaso, C., Carrascosa, A.V., *et al*. (2013) Tannic acid-dependent modulation of selected *Lactobacillus plantarum* traits linked to gastrointestinal survival. *PLoS One* **8:** e66473.

Rubinstein, M.R., Wang, X., Liu, W., Hao, Y., Cai, G., and Han, Y.W. (2013) Fusobacterium nucleatum promotes colorectal carcinogenesis by modulating E-cadherin/beta-catenin signaling via its FadA adhesin. *Cell Host Microbe* **14:** 195–206.

Schmidt, T.S.B., Hayward, M.R., Coelho, L.P., Li, S.S., Costea, P.I., Voigt, A.Y., *et al*. (2019) Extensive transmission of microbes along the gastrointestinal tract. *Elife* **8:** e42693.

Segata, N., Waldron, L., Ballarini, A., Narasimhan, V., Jousson, O., and Huttenhower, C. (2012) Metagenomic microbial community profiling using unique clade-specific marker genes. *Nat Methods* **9:** 811–814.

Singh, U., and Kollman, P.A. (1984) An approach to computing electrostatic charges for molecules. *J Comput Chem* **5:** 129–145.

Soda, K. (2011) The mechanisms by which polyamines accelerate tumor spread. *J Exp Clin Cancer Res* **30:** 95.

Sprenger, J., Svensson, B., Halander, J., Carey, J., Persson, L., and Al-Karadaghi, S. (2015) Three-dimensional structures of *Plasmodium falciparum* spermidine synthase with bound inhibitors suggest new strategies for drug design. *Acta Crystallogr D Biol Crystallogr* **71:** 484–493.

Tomás-Cortázar, J., Plaza-Vinuesa, L., de las Rivas, B., Lavín, J.L., Barriales, D., Abecia, L., *et al*. (2018) Identification of a highly active tannase enzyme from the oral pathogen *Fusobacterium nucleatum* subsp. *polymorphum*. *Microb Cell Fact* **17:** 33.

Wang, J., Wolf, R.M., Caldwell, J.W., Kollman, P.A., and Case, D.A. (2004) Development and testing of a general amber force field. *J Comput Chem* **25:** 1157–1174.

Wu, M., Peng, X., Wen, H., Wang, Q., Chen, Q., McKinstry, W.J., and Ren, B. (2013) Expression, purification, crystallization and preliminary X-ray analysis of tannase from *Lactobacillus plantarum*. *Acta Crystallogr Sect F Struct Biol Cryst Commun* **69:** 456–459.

Yachida, S., Mizutani, S., Shiroma, H., Shiba, S., Nakajima, T., Sakamoto, T., *et al*. (2019) Metagenomic and metabolomic analyses reveal distinct stage-specific phenotypes of the gut microbiota in colorectal cancer. *Nat Med* **25:** 968–976.

Yamaoka, Y., Suehiro, Y., Hashimoto, S., Hoshida, T., Fujimoto, M., Watanabe, M., *et al*. (2018) *Fusobacterium nucleatum* as a prognostic marker of colorectal cancer in a Japanese population. *J Gastroenterol* **53:** 517–524.

Zeller, G., Tap, J., Voigt, A.Y., Sunagawa, S., Kultima, J.R., Costea, P.I., *et al*. (2014) Potential of fecal microbiota for early-stage detection of colorectal cancer. *Mol Syst Biol* **10:** 766.

Supporting information

Additional supporting information may be found online in the Supporting Information section at the end of the article.

Fig. S1. Genetic context of the tannase gene (FN_0616) within the *F. nucleatum subsp. nucleatum* 25586 genome.

Fig. S2. $TanB_{Fnn}$ is monomeric in solution.

Fig. S3. $TanB_{Fnn}$ substrate specificity.

Fig. S4. Biochemical properties of $TanB_{Fnn}$.

Fig. S5. Amino acid sequence and active site comparisons between $TanB_{Fnn}$ and $TanA_{Lp}$.

Fig. S6. Representative snapshots of three different 1 microsecond MD simulations of ethyl gallate (EG, in red) bound to $TanB_{Fnn}$.

Fig. S7. Representation of MD simulations of methyl digallate (MDG, in red) bound to $TanB_{Fnn}$.

Fig. S8. SPD interacts with $TanB_{Fnn}$.

Fig. S9. Structure of spermidine and its N1 and N8-acetylated derivatives in their charged form at neutral pH.

Fig. S10. Multiple sequence alignment of $TanB_{Fnn}$ with homologs found within the Fusobacteriales, particularly, from the genus *Leptotrichia: Leptotrichia sp.* OH3620_COT-345 (WP_125237392.1); *L. wadei* (WP_146961278.1); *L. massiliensis* (WP_071123737.1); *L. buccalis* (WP_157859547.1).

Fig. S11. Multiple sequence alignment of $TanB_{Fnn}$ with homologs from bacterial genera that are prevalent in the oral cavity: *Aggregatibacter* (WP_006718097.1); *Selenomonas* (WP_051586482.1); *Veillonella* (WP_127058572.1); *Mitsuokella* (WP_118475533.1).

Fig. S12. Multiple sequence alignment of $TanB_{Fnn}$ with homologs from bacterial genera present in the human gut: *Leptotrichia* (WP_157859547.1); *Veillonella* (WP_127058572.1); *Megasphaera* (WP_044503365.1); *Roseburia* (WP_173884414.1); *Bacteroides* (WP_164733466.1); *Parabacteroides* (WP_172733427.1); *Lachnoclostridium* (WP_087219107.1); *Fusicatenibacter* (WP_173816499.1); Dorea (WP_161159564.1); Blautia (WP_095175021.1); Lactobacillaceae (WP_054397147.1); Sutterella (GenBank: RGU74189.1).

Table S1 (related to Figure 1). Species harboring orthologous tannase proteins.

